



**HAL**  
open science

## **An image-based four-source surface energy balance model to estimate crop evapotranspiration from solar reflectance/thermal emission data (SEB-4S)**

Olivier Merlin, Jonas Chirouze, Albert Olioso, Lionel Jarlan, Ghani Chehbouni,  
Gilles Boulet

### ► **To cite this version:**

Olivier Merlin, Jonas Chirouze, Albert Olioso, Lionel Jarlan, Ghani Chehbouni, et al.. An image-based four-source surface energy balance model to estimate crop evapotranspiration from solar reflectance/thermal emission data (SEB-4S). *Agricultural and Forest Meteorology*, 2014, 184, pp.188-203. <10.1016/j.agrformet.2013.10.002>. <hal-00922053>

**HAL Id: hal-00922053**

**<https://hal.science/hal-00922053v1>**

Submitted on 23 Dec 2013

**HAL** is a multi-disciplinary open access archive for the deposit and dissemination of scientific research documents, whether they are published or not. The documents may come from teaching and research institutions in France or abroad, or from public or private research centers.

L'archive ouverte pluridisciplinaire **HAL**, est destinée au dépôt et à la diffusion de documents scientifiques de niveau recherche, publiés ou non, émanant des établissements d'enseignement et de recherche français ou étrangers, des laboratoires publics ou privés.



HAL Authorization

# An image-based four-source surface energy balance model to estimate crop evapotranspiration from solar reflectance/thermal emission data (SEB-4S)

Olivier Merlin<sup>\*,a</sup>, Jonas Chirouze<sup>a</sup>, Albert Olioso<sup>b</sup>, Lionel Jarlan<sup>a</sup>, Ghani Chehbouni<sup>a</sup>, Gilles Boulet<sup>a</sup>

<sup>a</sup>*Centre d'Etudes Spatiales de la Biosphère (CESBIO UMR5126), 31401 Toulouse, France*

<sup>b</sup>*INRA, EMMAH UMR1114, 84914 Avignon, France  
UAPV, EMMAH UMR1114, 84000 Avignon, France*

---

## Abstract

A remote sensing-based surface energy balance model is developed to explicitly represent the energy fluxes of four surface components of agricultural fields including bare soil, unstressed green vegetation, non-transpiring green vegetation, and standing senescent vegetation. Such a four-source representation (SEB-4S) is achieved by a consistent physical interpretation of the edges and vertices of the polygon (named  $T - f_{vg}$  polygon) obtained by plotting surface temperature ( $T$ ) as a function of fractional green vegetation ( $f_{vg}$ ) and the polygon (named  $T - \alpha$  polygon) obtained by plotting  $T$  as a function of surface albedo ( $\alpha$ ). To test the performance of SEB-4S, a  $T - \alpha$  image-based model and a  $T - f_{vg}$  image-based model are implemented as benchmarks. The three models are tested over a 16 km by 10 km irrigated area in north-western Mexico during the 2007-2008 agricultural season. Input data are composed of ASTER (Advanced Spaceborne Thermal Emission and Reflec-

---

\*telephone: +33 561556638; fax: +33 561558500; email: olivier.merlin@cesbio.cnes.fr

tion Radiometer) thermal infrared, Formosat-2 shortwave, and station-based meteorological data. The fluxes simulated by SEB-4S, the  $T - \alpha$  image-based model, and the  $T - f_{vg}$  image-based model are compared on seven ASTER overpass dates with the in situ measurements collected at six locations within the study domain. The evapotranspiration simulated by SEB-4S is significantly more accurate and robust than that predicted by the models based on a single (either  $T - f_{vg}$  or  $T - \alpha$ ) polygon. The improvement provided with SEB-4S reaches about  $100 \text{ W m}^{-2}$  at low values and about  $100 \text{ W m}^{-2}$  at the seasonal peak of evapotranspiration as compared with both the  $T - \alpha$  and  $T - f_{vg}$  image-based models. SEB-4S can be operationally applied to irrigated agricultural areas using high-resolution solar/thermal remote sensing data, and has potential to further integrate microwave-derived soil moisture as additional constraint on surface soil energy and water fluxes.

*Key words:* Evapotranspiration, thermal, reflectance, temperature, albedo, partitioning, irrigation.

---

## 1. Introduction

Evapotranspiration (ET) plays a crucial role in predicting soil water availability (Oki and Kanae, 2006), in flood forecasting (Bouilloud et al., 2010), in rainfall forecasting (Findell et al., 2011) and in projecting changes in the occurrence of heatwaves (Seneviratne et al., 2006) and droughts (Sheffield and Wood, 2008). The partitioning of ET into its surface components including soil evaporation, plant transpiration and canopy evaporation is important for modeling vegetation water uptake, land-atmosphere interactions and climate simulations. Large bare or partially covered soil surfaces especially occur in

10 many cultivated areas. The soil evaporation term corresponds to the por-  
11 tion of ET that is unusable for crop productivity (Wallace, 2000) and its  
12 participation as a component of water balance may become dominant over  
13 bare or partially vegetated soils (Allen et al., 1998). Moreover, knowledge of  
14 ET partitioning would provide a powerful constraint on the physics of land  
15 surface models (Gutmann and Small, 2007). However, field measurements of  
16 both soil evaporation and plant transpiration are very sparse, and the current  
17 solar/thermal remote sensing techniques do not fully address the partition-  
18 ing issue. This is notably due to the difficulty in separating the soil and  
19 vegetation components at the different phenological stages of crops from re-  
20 flectance and thermal infrared data alone (Moran et al., 1994; Merlin et al.,  
21 2010, 2012a).

22 A number of models have been developed to estimate ET from ther-  
23 mal remote sensing data (Courault et al., 2005; Gowda et al., 2008). Actual  
24 ET has been estimated by weighting the potential ET using reflectance-  
25 derived fractional photosynthetically-active (green) vegetation cover ( $f_{vg}$ )  
26 (Allen et al., 1998; Cleugh et al., 2007).  $f_{vg}$ -based modeling approaches are  
27 useful to provide ET estimates over integrated time periods e.g. the agri-  
28 cultural season. The point is that  $f_{vg}$  is not sensitive to vegetation water  
29 stress until there is actual reduction in biomass or changes in canopy geome-  
30 try (Gonzalez-Dugo et al., 2009). As a result  $f_{vg}$ -based ET methods are not  
31 adapted to operational irrigation management when the objective is to de-  
32 tect the onset of water stress. Instead, canopy temperature can detect crop  
33 water deficit (Idso et al., 1981; Jackson et al., 1981). Operational ET mod-  
34 els have hence been developed to monitor ET and soil moisture status from

35 remotely sensed surface temperature ( $T$ ) (Boulet et al., 2007; Hain et al.,  
36 2009; Anderson et al., 2012). Note that  $T$ -based ET models may also use  $f_{vg}$   
37 to partition soil and vegetation components (Norman et al., 1995), and sur-  
38 face albedo ( $\alpha$ ) as additional constraint on net radiation (Bastiaanssen et al.,  
39 1998). Among the  $T$ -based ET methods reviewed in Kalma et al. (2008)  
40 and Kustas and Anderson (2009), one can distinguish the single-source mod-  
41 els (Bastiaanssen et al., 1998; Su, 2002, e.g.) and the two-source models  
42 (Moran et al., 1994; Norman et al., 1995, e.g.), which implicitly and explic-  
43 itly represent soil evaporation and plant transpiration, respectively. Al-  
44 though both model representations may perform similarly in terms of ET  
45 estimates given they are correctly calibrated (Timmermans et al., 2007), the  
46 two-source models are of particular interest for ET partitioning.

47 Among  $T$ -based two-source ET models, one can distinguish the residual-  
48 based models (Norman et al., 1995; Anderson et al., 2007; Cammalleri et al.,  
49 2012, e.g.), which estimate ET as the residual term of an aerodynamic  
50 resistance surface energy balance equation, and the image-based models  
51 (Moran et al., 1994; Roerink et al., 2000; Long and Singh, 2012, e.g.), which  
52 estimate ET as a fraction (named surface evaporative efficiency or EE) of po-  
53 tential ET (Moran et al., 1994), or as a fraction (named surface evaporative  
54 fraction or EF) of available energy (Roerink et al., 2000; Long and Singh,  
55 2012). In image-based models, EF (or EE) is estimated as the ratio of  
56 the maximum to actual surface temperature difference to the maximum  
57 to minimum surface temperature difference. In Moran et al. (1994) and  
58 Long and Singh (2012), maximum and minimum temperatures are estimated  
59 over the dry and wet surface edges of a polygon drawn in the  $T - f_{vg}$  space,

60 respectively. In Roerink et al. (2000), maximum and minimum tempera-  
61 tures are estimated over the dry and wet surface lines drawn in the  $T - \alpha$   
62 space, respectively. As clearly stated by Tang et al. (2010), the advantages  
63 of image-based models over the residual-based models are 1) absolute high  
64 accuracy in remotely sensed  $T$  retrieval and atmospheric correction are not  
65 indispensable, 2) complex parameterization of aerodynamic resistance and  
66 uncertainty originating from replacement of aerodynamic temperature by re-  
67 motely sensed  $T$  is bypassed 3) no ground-based near surface measurements  
68 are needed other than remotely sensed  $T$ ,  $f_{vg}$  and  $\alpha$ , 4) a direct calculation  
69 of EF (or EE) can be obtained without resort to surface energy balance,  
70 and 5) estimations of EF (or EE) and available energy (or potential ET) are  
71 independent from each other by this method. Therefore, the overall errors  
72 in ET can be traced back to EF (EE) and available energy (potential ET)  
73 separately. Limitations of image-based models mainly lie in the determina-  
74 tion of the maximum and minimum surface temperatures. Specifically, the  
75 dry and wet edges can be placed accurately in the  $T - f_{vg}$  or  $T - \alpha$  space  
76 if 1) the full range of surface (soil moisture and vegetation cover) conditions  
77 is met within the study domain at the sensor resolution, 2) meteorological  
78 conditions are uniform in the study domain (Long et al., 2011, 2012), 3) the  
79 study domain is flat. In the case where all three conditions are not satisfied,  
80 alternative algorithms can be implemented to filter outliers in the  $T - f_{gv}$   
81 space (Tang et al., 2010), to estimate the maximum vegetation temperature  
82 from the  $T - \alpha$  space (Merlin et al., 2010, 2012b), to estimate extreme tem-  
83 peratures using a formulation of aerodynamic resistance (Moran et al., 1994;  
84 Long et al., 2012), or to correct remotely sensed  $T$  for topographic effects

85 (Merlin et al., 2013).

86 Moran et al. (1994) proposed the  $T - f_{vg}$  image-based water deficit index  
87 (WDI) to estimate a most probable range of crop water stress over partially-  
88 vegetated pixels. The different steps of the WDI method are: 1) the tem-  
89 peratures of the four vertices of the  $T - f_{vg}$  polygon are estimated using  
90 an energy balance model, 2) the minimum and maximum probable vegeta-  
91 tion temperatures are estimated from the measured composite  $T$ , together  
92 with the maximum and minimum simulated soil temperatures, and 3) the  
93 minimum and maximum probable water stress indices are computed by nor-  
94 malizing the minimum and maximum probable vegetation temperatures from  
95 the vegetation temperature extremes simulated by the energy balance model.  
96 Note that the WDI approach does not allow estimating a single crop water  
97 stress index value because the canopy temperature retrieval problem is ill-  
98 posed using solely  $T$  and  $f_{vg}$ . As mentioned in Moran et al. (1994) and  
99 Merlin et al. (2012a), knowledge of soil temperature would remove the un-  
100 derdetermination of the  $T - f_{vg}$  polygon approach. A second limitation of the  
101  $T - f_{vg}$  polygon approach is that  $f_{vg}$  does not allow distinguishing between  
102 soil and senescent vegetation, whereas the energy fluxes over bare soil and  
103 full-cover senescent vegetation may significantly differ. Separating vegetated  
104 areas according to the fraction of green versus senescent vegetation could be  
105 done by introducing additional information based on  $\alpha$  (Merlin et al., 2010)  
106 or a vegetation index such as the Cellulose Absorption Index (Nagler et al.,  
107 2003; Krapez and Oliosio, 2011). Note that optical data provide information  
108 on the surface skin only, which inherently prevents from separating green and  
109 senescent vegetation in the vertical dimension.

110 Roerink et al. (2000) proposed the Simplified Surface Energy Balance In-  
111 dex (S-SEBI) to estimate ET from the  $T - \alpha$  space. S-SEBI determines the  
112 wet and dry lines by interpreting the observed correlations between  $T$  and  $\alpha$   
113 (Menenti et al., 1989). The wet line is defined as the lower limit of the  $T - \alpha$   
114 space. It generally has a positive slope as a result of an evaporation control on  
115  $T$ . The dry line is defined as the upper limit of the  $T - \alpha$  space. It generally  
116 has a negative slope as a result of a radiation control on  $T$  (Roerink et al.,  
117 2000). One main advantage of the  $T - \alpha$  space over the  $T - f_{vg}$  space is that  
118  $\alpha$  is sensitive to the total vegetation cover including green and senescent veg-  
119 etation, whereas  $f_{vg}$  is sensitive to the green vegetation only (Merlin et al.,  
120 2010). One drawback is that unstressed green vegetation, non-transpiring  
121 vegetation and senescent vegetation are not easily separable in the  $T - \alpha$   
122 space, which makes identifying green crop water stress more difficult than  
123 using the  $T - f_{vg}$  space. Moreover the slope of both wet and dry lines may  
124 be difficult to determine when the full physical range of  $\alpha$  ( $\sim 0.1-0.4$ ) is not  
125 covered within the study domain.

126 Although  $T - f_{vg}$  and  $T - \alpha$  image-based models have been applied sepa-  
127 rately (Choi et al., 2009), or intercompared (Galleguillos et al., 2011), there  
128 is no model that combines the strength of each polygon notably in terms of  
129 ET partitioning. The objective of this study is thus to develop an image-  
130 based surface energy balance model (SEB-4S) that builds on advantages of  
131 both  $T - f_{vg}$  and  $T - \alpha$  spaces by 1) adequately constraining four surface  
132 components of agricultural fields including bare soil, unstressed green vegeta-  
133 tion, non-transpiring green vegetation and standing senescent vegetation, 2)  
134 partitioning ET into soil evaporation and unstressed green vegetation tran-

135 spiration, and 3) developing an automated algorithm for estimating tem-  
136 perature endmembers from joint  $T - f_{vg}$  and  $T - \alpha$  spaces. The modeling  
137 approach is tested over a 16 km by 10 km irrigated area in northwestern  
138 Mexico using ASTER (Advanced Spaceborne Thermal Emission and Reflec-  
139 tion Radiometer) and Formosat-2 data collected on seven dates during the  
140 2007-2008 agricultural season. Experimental data are described in Section  
141 2. SEB-4S is described in Section 3, and two common ( $T - f_{vg}$  and  $T - \alpha$ )  
142 image-based models are reminded in Section 4. In Section 5, the surface  
143 fluxes simulated by SEB-4S, the  $T - f_{vg}$  image-based model and the  $T - \alpha$   
144 image-based model are compared with in situ measurements at six locations.

## 145 **2. Data collection and pre-processing**

146 The Yaqui experiment was conducted from December 2007 to May 2008  
147 over an irrigated area (27.25°N, 109.88°W) in the Yaqui valley (Sonora State)  
148 in northwestern Mexico. The campaign focused on a 4 km by 4 km area in-  
149 cluding 50% of wheat, the other 50% being composed of beans, broccoli,  
150 chickpea, chili pepper, corn, orange, potatoes, safflower and sorghum. The  
151 objective of the experiment was to characterize the spatial variability of sur-  
152 face fluxes from the field (hectometric) to kilometeric scale. More details about  
153 the Yaqui experiment can be found in Merlin et al. (2010), Fieuzal et al.  
154 (2011) and Chirouze et al. (2013). In this paper, the study area is defined  
155 as a 16 km by 10 km area containing the 4 km by 4 km Yaqui experimental  
156 area and included in all satellite images. During the 2007-2008 agricultural  
157 season, 7 cloud-free ASTER images were collected over the Yaqui area at  
158 around 11:00 am local solar time on December 30, February 23, March 10,

159 April 11, April 27, May 6 and May 13 and 26 cloud-free Formosat-2 images  
160 were obtained from December 27, 2007 to May 13, 2008.

### 161 *2.1. Flux stations*

162 Seven micro-meteorological stations equipped with eddy covariance flux  
163 measurement system were installed in different fields. For each of the seven  
164 sites, the net radiation was acquired with CNR1 or Q7.1 (REBS) radiometers  
165 depending on the stations (see Table 1). The soil heat flux was estimated  
166 with HUKSEFLUX HFP-01 plates buried at 0.05 m at the top and bottom  
167 of the furrow (when applicable). Those data were acquired at a frequency of  
168 10 s and then averaged and recorded each 30 min. Latent and sensible heat  
169 fluxes were measured with KH20 fast response hygrometers (Campbell) and  
170 Campbell CSAT3 or RM Young 81000 3-D Sonic Anemometer at a frequency  
171 of 10 Hz and converted to 30 min average, respectively. Meteorological data  
172 including air temperature, solar radiation, relative humidity and wind speed  
173 were monitored throughout the agricultural season at a semi-hourly time step  
174 from December 27, 2007 until May 17, 2008. Details about the automated  
175 data acquisition and flux data quality can be found in Chirouze et al. (2013).  
176 In this paper, the six stations listed in Table 1 with at least four (among a  
177 total of seven) ASTER overpass dates of data including the four energy fluxes  
178 ( $Rn$ ,  $G$ ,  $LE$ ,  $H$ ) are used in the comparison analysis.

### 179 *2.2. ASTER thermal infrared data*

180 ASTER was launched in 1999 on a sun-synchronous platform (NASA's  
181 Terra satellite) with 11:00 am descending Equator crossing and a 16-day  
182 revisit cycle. The ASTER thermal sensor provides scenes of approximately

183 60 km by 60 km. Data are collected on request over specified areas. There  
184 are five thermal bands centered at 8.30, 8.65, 9.05, 10.60 and 11.63  $\mu\text{m}$  with  
185 a 90 m resolution. ASTER official products were downloaded from the Earth  
186 Observing System Data Gateway and extracted over the 16 km by 10 km  
187 study area.

### 188 *2.2.1. Surface temperature*

189 The 90 m resolution surface skin temperature ( $T$ ) retrieved by the “tem-  
190 perature and emissivity separation” algorithm (Gillespie et al., 1998; Schmugge et al.,  
191 1998) was used. The absolute registration of temperature data was performed  
192 using a background 8 m resolution Formosat-2 image (Merlin et al., 2010).

### 193 *2.2.2. Broad-band surface emissivity*

194 The 90 m resolution ASTER channel emissivity retrieved by the “temper-  
195 ature and emissivity separation” algorithm was used. The absolute registra-  
196 tion of emissivity data was set to that of temperature data on the same dates.  
197 The broad-band surface emissivity ( $\epsilon$ ) was expressed as a linear combination  
198 of ASTER channel emissivities using the coefficients in Ogawa and Schmugge  
199 (2004).

### 200 *2.3. Formosat-2 red and near-infrared data*

201 Formosat-2 is an Earth observation satellite launched in 2004 by the Na-  
202 tional Space Organization of Taiwan. It provides high (8 m) resolution im-  
203 ages of a particular area every day (9:30 am equator-crossing time) for four  
204 bands (blue, green, red and near-infrared) and with the same view angle  
205 (Chern et al., 2008). In this paper, the Formosat-2 data collected on the  
206 nearest date from each of the seven ASTER overpass dates were used to

207 estimate  $f_{vg}$  and  $\alpha$  from the red and near-infrared reflectances aggregated  
208 at ASTER thermal sensor resolution. The reason why Formosat-derived in-  
209 stead of ASTER-derived  $\alpha$  was used is mainly because the ASTER shortwave  
210 infrared data were unusable on four out of the seven ASTER overpass dates  
211 (Chirouze et al., 2013).

### 212 2.3.1. Fractional green vegetation cover

213 Fractional green (photosynthetically active) vegetation cover ( $f_{vg}$ ) is es-  
214 timated using the expression of Gutman and Ignatov (1998):

$$f_{vg} = \frac{\text{NDVI} - \text{NDVI}_{\mathbf{s}}}{\text{NDVI}_{\mathbf{vg}} - \text{NDVI}_{\mathbf{s}}} \quad (1)$$

215 with  $\text{NDVI}_{\mathbf{vg}}$  (for clarity all the variables defined at the 16 km by 10 km  
216 scale are written in bold) corresponding to fully-covering green vegetation  
217 and  $\text{NDVI}_{\mathbf{s}}$  to bare soil or to bare soil partially covered by senescent (non-  
218 photosynthetically active) vegetation. In the paper,  $\text{NDVI}_{\mathbf{vg}}$  and  $\text{NDVI}_{\mathbf{s}}$   
219 are set to the maximum (0.93) and minimum (0.18) value of the NDVI (Nor-  
220 malized Difference Vegetation Index) observed during the agricultural season  
221 within the study domain. NDVI is computed as the ratio of the difference  
222 between re-sampled Formosat-2 near-infrared and red reflectances to their  
223 sum.

### 224 2.3.2. Surface albedo

225 Surface albedo ( $\alpha$ ) is estimated as a weighted sum of re-sampled Formosat-  
226 2 red and near-infrared reflectances with the coefficients given by Weiss et al.  
227 (1999) and validated in Bsaibes et al. (2009), and in Chirouze et al. (2013)  
228 over the study area.

### 229 3. SEB-4S model

230 SEB-4S is based on the classical surface energy balance equation ap-  
231 plied to four surface components: bare soil, unstressed green vegetation,  
232 non-transpiring green vegetation and senescent vegetation. ET is computed  
233 as the sum of the four component latent heat fluxes. A key step in the  
234 modeling approach is therefore to estimate the component fractions. While  
235 subsections 3.1 and 3.2 set the physical basis of SEB-4S, the following sub-  
236 sections 3.3-7 translate the physical interpretation of both  $T - \alpha$  and  $T - f_{vg}$   
237 spaces into geometrical problems for solving the four component fractions.  
238 Along this section, the reader may refer to the definition of component frac-  
239 tions in Table 2, and to the schematic chart presented in Figure 1.

#### 240 3.1. Surface energy balance

241 The surface energy balance can be written as:

$$Rn - G = H + LE \quad (2)$$

242 with  $Rn$  ( $\text{Wm}^{-2}$ ) being the surface net radiation,  $G$  ( $\text{Wm}^{-2}$ ) the ground  
243 heat flux,  $H$  ( $\text{Wm}^{-2}$ ) the surface sensible heat flux and  $LE$  ( $\text{Wm}^{-2}$ ) the  
244 surface latent heat flux. In SEB-4S, the surface net radiation is decomposed  
245 into four components:

$$Rn = Rn_s + Rn_{vgu} + Rn_{vgn} + Rn_{vss} \quad (3)$$

246 with  $Rn_s$  ( $\text{Wm}^{-2}$ ) being the soil net radiation,  $Rn_{vgu}$  ( $\text{Wm}^{-2}$ ) the net  
247 radiation of unstressed green vegetation,  $Rn_{vgn}$  ( $\text{Wm}^{-2}$ ) the net radiation

248 of non-transpiring green vegetation, and  $Rn_{vss}$  ( $\text{Wm}^{-2}$ ) the net radiation of  
249 standing senescent vegetation.

250 Component net radiations are estimated as a fraction of surface net ra-  
251 diation:

$$Rn_i = f_i Rn \quad (4)$$

252 with  $f_i$  (-) being the fraction of  $i$  component, with  $i = s, vgu, vgn$  and  
253  $vss$ .

254 The decomposition of surface sensible heat flux into four components  
255 gives:

$$H = H_s + H_{vgu} + H_{vgn} + H_{vss} \quad (5)$$

256 with  $H_s$  ( $\text{Wm}^{-2}$ ) being the soil sensible heat flux,  $H_{vgu}$  ( $\text{Wm}^{-2}$ ) the sen-  
257 sible heat flux over unstressed green vegetation,  $H_{vgn}$  ( $\text{Wm}^{-2}$ ) the sensible  
258 heat flux over non-transpiring green vegetation, and  $H_{vss}$  ( $\text{Wm}^{-2}$ ) the sensi-  
259 ble heat flux over standing senescent vegetation. We assume that the temper-  
260 ature of well-watered/unstressed green vegetation is close to air temperature  
261 meaning that the unstressed green vegetation sensible heat flux is neglected.  
262 This assumption is one of the main hypotheses of most contextual models  
263 such as S-SEBI (Roerink et al., 2000) or SEBAL (Bastiaanssen et al., 1998).  
264 SEB-4S is thus expected to overestimate sensible heat flux and reciprocally  
265 to underestimate ET in the case where leaf temperature is below air tem-  
266 perature especially under low vapor pressure deficit. Further developments  
267 of SEB-4S may address this issue by replacing EF with EE (Moran et al.,  
268 1994) or using the Priestley-Taylor formulation (Jiang and Islam, 1999).

269 Similarly, the decomposition of surface latent heat flux into four compo-  
 270 nents gives:

$$LE = LE_s + LE_{vgu} + LE_{vgn} + LE_{vss} \quad (6)$$

271 with  $LE_s$  ( $\text{Wm}^{-2}$ ) being the soil latent heat flux,  $LE_{vgu}$  ( $\text{Wm}^{-2}$ ) the  
 272 latent heat flux over unstressed green vegetation,  $LE_{vgn}$  ( $\text{Wm}^{-2}$ ) the latent  
 273 heat flux over non-transpiring green vegetation, and  $LE_{vss}$  ( $\text{Wm}^{-2}$ ) the latent  
 274 heat flux over standing senescent vegetation. Consistent with the definition  
 275 of non-transpiring green and senescent vegetation,  $LE_{vgn}$  and  $LE_{vss}$  are both  
 276 set to zero.

277 Over bare soil, the energy budget can be written as:

$$Rn_s - G = H_s + LE_s \quad (7)$$

278 with

$$LE_s = \text{SEF}(Rn_s - G) \quad (8)$$

279 with SEF being the soil evaporative fraction.

280 Over unstressed green vegetation, the energy budget can be written as:

$$Rn_{vgu} = LE_{vgu} \quad (9)$$

281 Over non-transpiring green vegetation, the energy budget can be written  
 282 as:

$$Rn_{vgn} = H_{vgn} \quad (10)$$

283 Over standing senescent vegetation, the energy budget can be written as:

$$Rn_{vss} = H_{vss} \quad (11)$$

284 Surface net radiation in Equation (4) is estimated as:

$$Rn = (1 - \alpha)R_g + \epsilon(R_a - \sigma T^4) \quad (12)$$

285 with  $R_g$  ( $\text{Wm}^{-2}$ ) being the incoming shortwave radiation,  $\sigma$  ( $\text{Wm}^{-2}\text{K}^{-4}$ )  
286 the Boltzmann constant, and  $R_a$  ( $\text{Wm}^{-2}$ ) the atmospheric longwave radiation  
287 computed as:

$$R_a = \epsilon_a \sigma T_a^4 \quad (13)$$

288 with  $T_a$  (K) being the air temperature, and  $\epsilon_a$  (-) the air emissivity esti-  
289 mated as in Brutsaert (1975):

$$\epsilon_a = 1.24 \left( \frac{e_a}{T_a} \right)^{0.143} \quad (14)$$

290 with  $e_a$  (hPa) being the air vapor pressure.

291 Two different expressions are proposed to estimate ground heat flux. A  
292 first formulation is given by Su (2002):

$$G = \Gamma Rn \quad (15)$$

293 with

$$\Gamma = \Gamma_{\mathbf{vg}} + (1 - f_{vg})(\Gamma_{\mathbf{s}} - \Gamma_{\mathbf{vg}}) \quad (16)$$

294 with  $\Gamma_{\mathbf{vg}}$  and  $\Gamma_{\mathbf{s}}$  being empirical parameters set to 0.05 (Monteith, 1973)  
 295 and 0.32 (Kustas and Daughtry, 1989) respectively (Su, 2002). To take ad-  
 296 vantage of the four-source representation of SEB-4S, a second formulation is  
 297 tested:

$$\Gamma' = \Gamma_{\mathbf{vg}} + (1 - f_{vgu} - f_s \text{SEF})(\Gamma_{\mathbf{s}} - \Gamma_{\mathbf{vg}}) \quad (17)$$

298 The physical rationale of  $\Gamma'$  is that  $G$  is expected to vary with soil tem-  
 299 perature gradient, which is inversely related to soil moisture availability. In  
 300 Equation (17), soil moisture availability is approximated by a first-guess EF  
 301 computed as  $f_{vgu} + f_s \text{SEF}$ . Note that  $\Gamma$  and  $\Gamma'$  formulations are equal in  
 302 the case where  $f_{vgn} = f_s \text{SEF}$ . Tanguy et al. (2012) have recently proposed a  
 303 parameterization of  $G$  as a function of EF consistent with Equation (17).

### 304 3.2. Model assumptions

305 The component fractions in Equation (4) and (17) and SEF in Equations  
 306 (8) and (17) are derived from seven endmembers: the soil temperature  $\mathbf{T}_{\mathbf{s},\mathbf{max}}$   
 307 corresponding to  $\text{SEF} = 0$ , the soil temperature  $\mathbf{T}_{\mathbf{s},\mathbf{min}}$  corresponding to  
 308  $\text{SEF} = 1$ , the temperature of well-watered/unstressed vegetation  $\mathbf{T}_{\mathbf{v},\mathbf{min}}$ , the  
 309 temperature of non-transpiring green or senescent vegetation  $\mathbf{T}_{\mathbf{v},\mathbf{max}}$ , the  
 310 soil albedo  $\alpha_{\mathbf{s}}$ , the green vegetation albedo  $\alpha_{\mathbf{vg}}$ , and the senescent vegetation  
 311 albedo  $\alpha_{\mathbf{vs}}$ . Below is a summary of the assumptions made in the following  
 312 subsections to derive the seven parameters from solar/thermal remote sensing  
 313 data.

314 The assumptions common to other image-based approaches such as WDI  
 315 and S-SEBI are:

- 316 • Atmospheric conditions are relatively homogeneous over the study area  
317 (Tang et al., 2010; Long and Singh, 2012, e.g.).
- 318 • The minimum temperature of green vegetation is close to air tempera-  
319 ture (Carlson et al., 1995; Prihodko and Goward, 1997; Bastiaanssen et al.,  
320 1998). Note that this assumption relates both to well-watered green  
321 vegetation, which may have a physical temperature slightly below air  
322 temperature due to the evaporation of intercepted water and/or ad-  
323 vection phenomenon, and to unstressed (fully transpiring) vegetation,  
324 which may have a physical temperature slightly above air temperature  
325 due to minimum stomatal resistance.
- 326 • The four temperature endmembers are representative of extreme con-  
327 ditions over the study area at the time of thermal sensor overpass. This  
328 notably implies that the aerodynamic resistance to heat transfer is as-  
329 sumed to be approximately uniform by fractional vegetation cover class.  
330 Although this assumption is implicit in all image-based algorithms, it  
331 is rarely mentioned in the literature.
- 332 • The impact of the spatial variability of surface soil moisture (Idso et al.,  
333 1975) and roughness (Matthias et al., 2000) on soil albedo is neglected,  
334 meaning that the soil albedo over dry or wet soil surfaces can be ap-  
335 proximated to  $\alpha_s$ . This assumption is implicit in S-SEBI because the  
336 EF is computed for a fixed (not variable)  $\alpha$  value (Roerink et al., 2000).
- 337 • Component temperatures are linearly related to component fractions  
338 (Merlin and Chehbouni, 2004; Anderson et al., 2007; Long and Singh,  
339 2012).

340 The three assumptions specific to SEB-4S are:

- 341 •  $\alpha_{\mathbf{vg}}$  is approximately the same for different crops. Green crop albedo  
342 varies mainly within 0.16-0.22, with a mean value of about 0.19 (Kondratyev et al.,  
343 1982; Hansen, 1993; Campbell and Norman, 1998).
- 344 •  $\alpha_{\mathbf{s}}$  is not larger than  $\alpha_{\mathbf{vg}}$ . As described in the following subsections, the  
345 assumption  $\alpha_{\mathbf{s}} \leq \alpha_{\mathbf{vg}}$  is essential for drawing the polygon in the  $T - \alpha$   
346 space. This assumption generally applies to brown agricultural soils,  
347 especially to the Yaqui area where the top 0-20 cm soil was classified  
348 as clay. Soil albedo typically ranges from 0.08 to 0.14 for clay and from  
349 0.10 to 0.20 for clay loam (Ten Berge, 1986). Further developments  
350 of SEB-4S will integrate the effects of bright soils (e.g. sands) in the  
351 modelling approach.
- 352 •  $\alpha_{\mathbf{vs}}$  is larger than  $\alpha_{\mathbf{vg}}$ . Most plants change color when they mature and  
353 enter senescence stage, which is generally associated with an increase of  
354 vegetation albedo under dry conditions (Kondratyev et al., 1982). In  
355 particular, the albedo of cereal stubble (straw stalks left standing in the  
356 paddock) typically reaches values larger than 0.30 (Piggin and Schwerdtfeger,  
357 1973; Merlin et al., 2010).

### 358 3.3. Estimating albedo endmembers

359  $\alpha_{\mathbf{s}}$  is estimated as the minimum  $\alpha$  at the time of satellite overpass. The  
360 mean and standard deviation of  $\alpha_{\mathbf{s}}$  is estimated as 0.09 and 0.01 respec-  
361 tively, which is fully consistent with values reported in the literature for clay  
362 (Ten Berge, 1986).  $\alpha_{\mathbf{vg}}$  is estimated as the temporal mean (over different

363 dates) of the  $\alpha$  corresponding to the minimum  $T$  within the observation  
 364 scene ( $\alpha_{\mathbf{vg}} = 0.19$ ). Note that the standard deviation of daily green veg-  
 365 etation albedo is estimated as 0.03, which is fully consistent with values  
 366 reported in the literature for fully covering green crops (Kondratyev et al.,  
 367 1982; Hansen, 1993; Campbell and Norman, 1998).  $\alpha_{\mathbf{vs}}$  is estimated as the  
 368 maximum  $\alpha$  within the observation scene and for the entire agricultural sea-  
 369 son ( $\alpha_{\mathbf{vs}} = 0.39$ ). Note that the mean and standard deviation of daily max-  
 370 imum albedo is 0.29 and 0.07, respectively. The large temporal variability  
 371 of daily maximum albedo is explained by the great increase in  $\alpha$  during the  
 372 senescence period. Figure 2 plots  $T$  as a function of  $\alpha$  and illustrates the  
 373 location of  $\alpha_{\mathbf{s}}$ ,  $\alpha_{\mathbf{vg}}$ , and  $\alpha_{\mathbf{vs}}$  for  $T$  and  $\alpha$  data on 27 April 2008.

#### 374 3.4. Estimating temperature endmembers

375 The four temperature endmembers composed of  $\mathbf{T}_{\mathbf{s,max}}$ ,  $\mathbf{T}_{\mathbf{s,min}}$ ,  $\mathbf{T}_{\mathbf{v,min}}$ ,  
 376 and  $\mathbf{T}_{\mathbf{v,max}}$  are estimated by providing an original consistent interpretation  
 377 of the  $T - \alpha$  and  $T - f_{vg}$  polygons. In particular, a correspondance is built  
 378 between the four vertices of the  $T - \alpha$  and  $T - f_{vg}$  polygons as illustrated in  
 379 Figure 2 and explained below. For clarity, a schematic chart is presented in  
 380 Figure 3.

381 The four edges of the  $T - \alpha$  polygon are interpreted as “bare soil” between  
 382 **A** and **B**, “wet surface” between **B** and **C**, “full-cover vegetation” between  
 383 **C** and **D**, and “dry surface” between **D** and **A**. The four edges of the  $T - f_{vg}$   
 384 polygon are interpreted as “bare soil or mixed soil and senescent vegetation”  
 385 between **A** and **B**, “wet surface” between **B** and **C**, “full-cover green vege-  
 386 tation” between **C** and **D**, and “dry surface” between **D** and **A**. Note that  
 387 the segments [**AB**] and [**CD**] are interpreted differently in the  $T - \alpha$  and

388  $T - f_{vg}$  polygons cover because  $\alpha$  is a signature of total (green plus senescent)  
 389 vegetation cover while  $f_{vg}$  (via the NDVI) is a signature of green vegetation  
 390 cover only.

391 Each polygon can provide an estimate of the four temperature endmem-  
 392 bers. In the  $T - \alpha$  polygon,  $\mathbf{T}_{s,\max}$  can be set to the maximum  $T$ ,  $\mathbf{T}_{s,\min}$  to  
 393 the minimum  $T$  at minimum  $\alpha$ ,  $\mathbf{T}_{v,\min}$  to the minimum  $T$ , and  $\mathbf{T}_{v,\max}$  to  
 394 the  $T$  at maximum  $\alpha$ . Similarly, in the  $T - f_{vg}$  polygon,  $\mathbf{T}_{s,\max}$  can be set  
 395 to the maximum  $T$ ,  $\mathbf{T}_{s,\min}$  to the minimum  $T$  at minimum  $f_{vg}$ ,  $\mathbf{T}_{v,\min}$  to  
 396 the minimum  $T$ , and  $\mathbf{T}_{v,\max}$  to the maximum  $T$  at maximum  $f_{vg}$ . However,  
 397 a different approach is preferred herein to improve the robustness, especially  
 398 in the environments where all surface conditions (dry, wet, bare, full-cover)  
 399 are not necessarily met. In this paper, the procedure for automatically esti-  
 400 mating temperature endmembers is based on the consistency between both  
 401  $T - \alpha$  and  $T - f_{vg}$  polygons:

- 402 • in the  $T - \alpha$  polygon, estimates of the minimum soil temperature  
 403 ( $\mathbf{T}_{s,\min,1}$  at  $\alpha = \alpha_s$ ) and minimum vegetation temperature ( $\mathbf{T}_{v,\min,1}$   
 404 at  $\alpha = \alpha_{vg}$ ) are obtained by drawing a line passing through the two  
 405 points belonging to the “wet surface” edge, and estimates of maxi-  
 406 mum soil temperature ( $\mathbf{T}_{s,\max,1}$  at  $\alpha = \alpha_s$ ) and maximum vegetation  
 407 temperature ( $\mathbf{T}_{v,\max,1}$  at  $\alpha = \alpha_{vs}$ ) are obtained by drawing a line pass-  
 408 ing through the two points belonging to the “dry surface” edge. The  
 409 “wet surface” edge is defined as the line passing through the point  
 410 ( $\alpha_{vg}, \mathbf{T}_{\min}$ ), with  $\mathbf{T}_{\min}$  being the minimum  $T$ , and the point with  
 411  $\alpha < \alpha_{vg}$  and  $f_{vg} < \mathbf{f}_{vg,ENDMB}$  such as the slope of the line is max-  
 412 imum (meaning that all the other data points are located above the

413 “wet surface” edge).  $\mathbf{f}_{\mathbf{v}\mathbf{g},\mathbf{ENDMB}}$  is a threshold value (set to 0.5 in  
 414 this study) which stabilizes the determination of the slope. The use  
 415 of  $\mathbf{f}_{\mathbf{v}\mathbf{g},\mathbf{ENDMB}}$  is needed to avoid defining a line (the wet edge in this  
 416 case) from two data points very close together (Merlin et al., 2012b).  
 417 Similarly, the “dry surface” edge is defined as the line passing through  
 418 the point  $(\alpha_s, \mathbf{T}_{\mathbf{max}})$ , with  $\mathbf{T}_{\mathbf{max}}$  being the maximum  $T$ , and the point  
 419 with  $\alpha > \alpha_{\mathbf{v}\mathbf{g}}$  such as the slope of the line is maximum (meaning that  
 420 all the other data points are located below the “dry surface” edge).

- 421 • in the  $T - f_{vg}$  polygon, alternative estimates of the minimum soil tem-  
 422 perature ( $\mathbf{T}_{\mathbf{s},\mathbf{min},\mathbf{2}}$  at  $f_{vg} = 0$ ) and minimum vegetation temperature  
 423 ( $\mathbf{T}_{\mathbf{v},\mathbf{min},\mathbf{2}}$  at  $f_{vg} = 1$ ) are obtained by drawing a line passing through  
 424 the two points belonging to the “wet surface” edge, and alternative  
 425 estimates of maximum soil temperature ( $\mathbf{T}_{\mathbf{s},\mathbf{max},\mathbf{2}}$  at  $f_{vg} = 0$ ) and max-  
 426 imum vegetation temperature ( $\mathbf{T}_{\mathbf{v},\mathbf{max},\mathbf{2}}$  at  $f_{vg} = 1$ ) are obtained by  
 427 drawing a line passing through the two points belonging to the “dry  
 428 surface” edge. The “wet surface” edge is defined as the line passing  
 429 through the point  $(1, \mathbf{T}_{\mathbf{min}})$  and the point with  $f_{vg} < \mathbf{f}_{\mathbf{v}\mathbf{g},\mathbf{ENDMB}}$  such  
 430 as the slope of the line is maximum (meaning that all the other data  
 431 points are located above the “wet surface” edge). Similarly, the “dry  
 432 surface” edge is defined as the line passing through the point  $(0, \mathbf{T}_{\mathbf{max}})$   
 433 and the point with  $f_{vg} > \mathbf{f}_{\mathbf{v}\mathbf{g},\mathbf{ENDMB}}$  such as the slope of the line is  
 434 maximum (meaning that all the other data points are located below  
 435 the “dry surface” edge).

- 436 • an estimate of the four temperature endmembers is obtained by aver-

aging the two temperature endmembers sets 1 and 2:

$$\mathbf{T}_{s,\max} = \mathbf{T}_{s,\max,1} = \mathbf{T}_{s,\max,2} = \mathbf{T}_{\max} \quad (18)$$

$$\mathbf{T}_{s,\min} = (\mathbf{T}_{s,\min,1} + \mathbf{T}_{s,\min,2})/2 \quad (19)$$

$$\mathbf{T}_{v,\min} = \mathbf{T}_{v,\min,1} = \mathbf{T}_{v,\min,2} = \mathbf{T}_{\min} \quad (20)$$

$$\mathbf{T}_{v,\max} = (\mathbf{T}_{v,\max,1} + \mathbf{T}_{v,\max,2})/2 \quad (21)$$

### 438 3.5. Estimating component temperatures

439 Component temperatures are defined in Table 2. They are derived from  
 440 the temperature and albedo endmembers estimated previously. The green  
 441 vegetation temperature  $T_{vg}$  is computed from the  $T - f_{vg}$  polygon. The total  
 442 (green plus senescent) vegetation temperature  $T_v$  is computed from the  $T - \alpha$   
 443 polygon. The soil temperature  $T_s$  is computed as the residual term.

444 Component temperatures  $T_{vg}$  and  $T_v$  are estimated as the most probable  
 445 green and total vegetation temperature, respectively. Most probable tem-  
 446 peratures are defined as in the hourglass approach in Moran et al. (1994),  
 447 Merlin et al. (2012b) and Merlin et al. (2013). They correspond to the aver-  
 448 age of the minimum and maximum physically acceptable temperatures, given  
 449 the constraints imposed by the vertices of the polygons. Below is explained  
 450 how in practice the minimum and maximum acceptable green (or total) veg-  
 451 etation temperatures are determined from the location of a given data point

452  $(f_{vg}, T)$  in the  $T - f_{vg}$  space (or from the location of a given data point  $(\alpha, T)$   
 453 in the  $T - \alpha$  space).

454 *3.5.1. Estimating  $T_{vg}$  in the  $T - f_{vg}$  polygon*

455 By plotting the diagonals of the quadrilateral defined in the  $T - f_{vg}$   
 456 space, four areas are distinguished (Merlin et al., 2012b). The procedure  
 457 for estimating  $T_{vg}$  from the  $T - f_{vg}$  polygon is illustrated in Figure 4 and  
 458 described below:

- 459 • For a given data point located in zone Z1:

$$T_{vg} = (\mathbf{T}_{\mathbf{v},\min} + \mathbf{T}_{\mathbf{v},\max})/2 \quad (22)$$

- 460 • For a given data point located in zone Z2:

$$T_{vg} = (\mathbf{T}_{\mathbf{v},\min} + T_{vg,max})/2 \quad (23)$$

461 with  $T_{vg,max}$  being the green vegetation temperature associated with  
 462  $f_{vss} = 0$  and  $\text{SEF} = 1$  ( $T_s = \mathbf{T}_{\mathbf{s},\min}$ ).

- 463 • For a given data point located in zone Z3:

$$T_{vg} = (T_{vg,min} + T_{vg,max})/2 \quad (24)$$

464 with  $T_{vg,min}$  being the green vegetation temperature associated with  
 465  $f_{vss} = 0$  and  $\text{SEF} = 0$  ( $T_s = \mathbf{T}_{\mathbf{s},\max}$ ).

- 466 • For a given data point located in zone Z4:

$$T_{vg} = (T_{vg,min} + \mathbf{T}_{v,max})/2 \quad (25)$$

467 In zone Z1,  $T$  is mainly controlled by  $T_s$  (via soil evaporation) and the associ-  
 468 ated  $T_{vg}$  is uniform. In zone Z3,  $T$  is mainly controlled by  $T_{vg}$  (via vegetation  
 469 transpiration) and the associated  $T_s$  is uniform. In zones Z2 and Z4,  $T$  is  
 470 controlled by both  $T_s$  and  $T_{vg}$  (Merlin et al., 2012b).

471 *3.5.2. Estimating  $T_v$  in the  $T - \alpha$  polygon*

472 The  $T - \alpha$  polygon is used to estimate  $T_v$ . The rationale for choosing  
 473 the  $T - \alpha$  instead of the  $T - f_{vg}$  polygon is that  $\alpha$  is sensitive to both  
 474 green and senescent vegetation whereas  $f_{vg}$  (via NDVI) does not differentiate  
 475 between soil and senescent vegetation (Merlin et al., 2010). The procedure  
 476 for estimating  $T_v$  from the  $T - \alpha$  polygon is similar to the hourglass approach.  
 477 It is illustated in Figure 5 and described below:

- 478 • For a given data point located in zone Z1:

$$T_v = (\mathbf{T}_{v,min} + \mathbf{T}_{v,max})/2 \quad (26)$$

- 479 • For a given data point located in zone Z2, vegetation temperature is:

$$T_v = (\mathbf{T}_{v,min} + T_{v,max})/2 \quad (27)$$

480 with  $T_{v,max}$  being the vegetation temperature associated with SEF = 1  
 481 ( $T_s = \mathbf{T}_{s,min}$ ).

- 482 • For a given data point located in zone Z3:

$$T_v = (T_{v,min} + T_{v,max})/2 \quad (28)$$

483 with  $T_{v,min}$  being the vegetation temperature associated with SEF = 0  
 484 ( $T_s = \mathbf{T}_{s,max}$ ).

- 485 • For a given data point located in zone Z4:

$$T_v = (T_{v,min} + \mathbf{T}_{v,max})/2 \quad (29)$$

### 486 3.5.3. Estimating $T_s$

487  $T_s$  is estimated as the residual term:

$$T_s = \frac{T - f_v T_v}{1 - f_v} \quad (30)$$

488 Soil temperature from Equation (30) is expected to be more accurate for  
 489  $f_v \leq 0.5$  than for  $f_v > 0.5$ , and is undetermined for  $f_v = 1$ . In particular,  
 490 the soil temperature may get unphysical large values when  $f_v$  is close to 1.  
 491 To make the algorithm numerically stable, the upper limit of retrieved  $T_s$  is  
 492 set to  $\mathbf{T}_{s,max}$ . Note that uncertainties in  $T_s$  for large  $f_v$  values do not impact  
 493 ET estimates because  $f_s$  is close to zero in this case.

### 494 3.6. Estimating SEF

495 SEF in Equations (8) and (17) is estimated as:

$$SEF = \frac{\mathbf{T}_{s,max} - T_s}{\mathbf{T}_{s,max} - \mathbf{T}_{s,min}} \quad (31)$$

496 3.7. *Estimating component fractions*

497 The four component fractions  $f_s$ ,  $f_{vgu}$ ,  $f_{vgn}$ , and  $f_{vss}$  in Equation (4) are  
 498 derived by solving four equations.

499 Green vegetation fractions  $f_{vgu}$  and  $f_{vgn}$  are expressed as a function of  
 500  $f_{vg}$ ,  $T_{vg}$  and vegetation temperature endmembers:

$$f_{vg}T_{vg} = f_{vgu}\mathbf{T}_{\mathbf{v},\min} + f_{vgn}\mathbf{T}_{\mathbf{v},\max} \quad (32)$$

501 with  $T_{vg}$  being computed in Equations (22-25). Since  $f_{vgu} + f_{vgn} = f_{vg}$ ,  
 502 one is able to solve  $f_{vgu}$ :

$$f_{vgu} = \frac{\mathbf{T}_{\mathbf{v},\max} - T_{vg}}{\mathbf{T}_{\mathbf{v},\max} - \mathbf{T}_{\mathbf{v},\min}} f_{vg} \quad (33)$$

503 and  $f_{vgn}$ :

$$f_{vgn} = f_{vg} - f_{vgu} \quad (34)$$

504 The total fractional vegetation cover  $f_v$  (equal to  $f_{vgu}$  plus  $f_{vgn}$  plus  $f_{vss}$ )  
 505 is expressed as a function of  $T_v$ ,  $\alpha$ , and albedo and temperature endmembers.  
 506 In Figure 6,  $f_v$  is equal to the ratio IJ/IK with J being located at  $(\alpha, T)$ , I  
 507 located at  $(\alpha_s, T_s)$ , and K located at  $(\alpha_v, T_v)$  with  $\alpha_v$  being the vegetation  
 508 albedo, and  $T_v$  the vegetation temperature computed in Equations (26-29).  
 509 Both I and K are placed on the polygon of Figure 6 using the same approach  
 510 adopted to compute  $T_v$ . Given that  $(\mathbf{AB})$  is parallel to y-axis, one can deduce  
 511 that:

$$f_v = \frac{\alpha - \alpha_s}{\alpha_v - \alpha_s} \quad (35)$$

512 with  $\alpha_v$  being a function of  $T_v$ . On the full-cover edge [CD], one writes:

$$T_v = \mathbf{T}_{\mathbf{v},\min} + \frac{\alpha_v - \alpha_{\mathbf{v}\mathbf{g}}}{\alpha_{\mathbf{v}\mathbf{s}} - \alpha_{\mathbf{v}\mathbf{g}}} (\mathbf{T}_{\mathbf{v},\max} - \mathbf{T}_{\mathbf{v},\min}) \quad (36)$$

513 By inverting Equation (36), one obtains:

$$\alpha_v = \alpha_{\mathbf{v}\mathbf{g}} + \frac{T_v - \mathbf{T}_{\mathbf{v},\min}}{\mathbf{T}_{\mathbf{v},\max} - \mathbf{T}_{\mathbf{v},\min}} (\alpha_{\mathbf{v}\mathbf{s}} - \alpha_{\mathbf{v}\mathbf{g}}) \quad (37)$$

514 Hence,  $f_v$  is derived by injecting Equation (37) into Equation (35).

515  $f_{vss}$  is estimated as the residual term of  $f_v$ :

$$f_{vss} = f_v - f_{vg} \quad (38)$$

516  $f_s$  is estimated as the residual term:

$$f_s = 1 - f_v \quad (39)$$

#### 517 4. Image-based models

518 Two common image-based models are implemented as benchmarks to  
 519 evaluate the performance of SEB-4S in estimating EF/ET. Although the  
 520  $T - \alpha$  image-based model is similar to S-SEBI and the  $T - f_{vg}$  image-based  
 521 model similar to WDI, the objective is not to intercompare SEB-4S, S-SEBI  
 522 and WDI, but rather to compare SEB-4S with image-based ET models having  
 523 the same general structure as SEB-4S. In particular, the wet and dry edges  
 524 are determined from the same temperature endmembers set in each case,  
 525 and both image-based models express ET as a function of EF as in SEB-4S  
 526 (instead of EE for WDI).

527 *4.1.  $T - \alpha$  image-based model*

528 The  $T - \alpha$  image-based model is derived from S-SEBI (Roerink et al.,  
 529 2000). In S-SEBI, linear relationships are established between  $T$  and  $\alpha$  for  
 530 the wet and the dry surface cases. The wet and dry surface lines are defined  
 531 as the lower and upper limit of the  $T - \alpha$  space, respectively. In this study,  
 532 the wet and dry lines are set to **(CD)** and **(AD)**, respectively (see Figure  
 533 2). ET is then estimated as EF times the surface available energy ( $Rn - G$ ),  
 534 with EF being computed as:

$$\text{EF} = \frac{T_{max} - T}{T_{max} - T_{min}} \quad (40)$$

535 with  $T_{max}$  being the  $T$  if the pixel surface was fully dry, and  $T_{min}$  the  $T$   
 536 if the pixel surface was fully wet.  $T_{max}$  and  $T_{min}$  are computed at  $\alpha$  on the  
 537 dry and wet line, respectively (see Figure 7a).

538 *4.2.  $T - f_{vg}$  image-based model*

539 The  $T - f_{vg}$  image-based model is derived from the WDI (Moran et al.,  
 540 1994). In WDI, linear relationships are established between  $T$  and  $f_{vg}$  for  
 541 the wet and the dry surface cases. The wet and dry surface lines are defined  
 542 as the lower and upper limit of the  $T - f_{vg}$  space, respectively. In this study,  
 543 the wet and dry lines are set to **(BC)** and **(AD)**, respectively (see Figure 2).  
 544 In WDI, ET is estimated as:

$$LE = (1 - \text{WDI})LEp \quad (41)$$

545 with  $LEp$  ( $\text{Wm}^{-2}$ ) being the potential ET. Herein,  $LEp$  is replaced by  
 546  $Rn - G$  in Equation (41) to be consistent with both SEB-4S and the  $T - \alpha$

547 image-based model. The factor  $(1 - \text{WDI})$  is estimated as EF in Equation  
548 (40) with  $T_{max}$  and  $T_{min}$  being computed at  $f_{vg}$  on the dry and wet line,  
549 respectively (see Figure 7b).

## 550 5. Application

551 The simulation results of SEB-4S, the  $T - \alpha$  image-based model, and  
552 the  $T - f_{vg}$  image-based model are compared with the in situ measurements  
553 collected by the six flux stations. The objective is to evaluate model perfor-  
554 mances in terms of ET estimates in a range of surface conditions. Compar-  
555 isons are made at the pixel scale by extracting the ASTER thermal pixels  
556 including a flux station.

### 557 5.1. Temperature endmembers and component fractions

558 The algorithm for estimating temperature endmembers is run on the  
559 seven ASTER overpass dates. To assess the consistency between the tem-  
560 perature endmembers set 1 (derived from the  $T - \alpha$  polygon) and 2 (de-  
561 rived from the  $T - f_{vg}$  polygon), Figure 8 plots  $\mathbf{T}_{s,\min,2}$  versus  $\mathbf{T}_{s,\min,1}$  and  
562  $\mathbf{T}_{v,\max,2}$  versus  $\mathbf{T}_{v,\max,1}$  (remind that by definition  $\mathbf{T}_{s,\max,2} = \mathbf{T}_{s,\max,1}$  and  
563  $\mathbf{T}_{v,\min,2} = \mathbf{T}_{v,\min,1}$ ). In terms of minimum soil temperature, temperature  
564 endmembers sets 1 and 2 are remarkably consistent with a correlation co-  
565 efficient and slope of the linear regression between  $\mathbf{T}_{s,\min,2}$  and  $\mathbf{T}_{s,\min,1}$  of  
566 0.91 and 0.83, respectively. In terms of maximum vegetation temperature,  
567 temperature endmembers sets 1 and 2 are still consistent but the difference  
568 between both data sets is larger with a correlation coefficient and slope of the  
569 linear regression between  $\mathbf{T}_{v,\max,2}$  and  $\mathbf{T}_{v,\max,1}$  of 0.50 and 0.39, respectively.  
570 Overall the temperature endmembers estimated from the  $T - \alpha$  and  $T - f_{vg}$

571 polygons have an absolute mean difference of  $0.5^{\circ}\text{C}$  and  $2.5^{\circ}\text{C}$  for  $\mathbf{T}_{s,\min}$  and  
572  $\mathbf{T}_{v,\max}$ , respectively. These results justify the strategy to derive  $\mathbf{T}_{s,\min}$  and  
573  $\mathbf{T}_{v,\max}$  from the average of temperature endmembers sets 1 and 2.

574 Figure 9 plots side by side the  $T - \alpha$  and  $T - f_{vg}$  spaces overlaid with the  
575 polygons drawn from the retrieved temperature endmembers  $\mathbf{T}_{s,\max}$ ,  $\mathbf{T}_{s,\min}$ ,  
576  $\mathbf{T}_{v,\min}$  and  $\mathbf{T}_{v,\max}$ . One observes that the shape of both the  $T - \alpha$  and  
577  $T - f_{vg}$  spaces significantly varies from date to date. In particular, the  
578 shape of the  $T - \alpha$  space at the end (on 13 May 2008) and at the beginning  
579 (on 30 December 2007) of the agricultural season are very distinct due to  
580 a different range of  $\alpha$  values. This is notably explained by the presence  
581 of bright senescent vegetation towards the end of the agricultural season.  
582 However, despite the strong temporal variability of  $T - \alpha$  spaces, the  $T - \alpha$   
583 polygons automatically retrieved by the temperature endmembers algorithm  
584 are relatively stable, meaning that the four edges are robustly estimated  
585 across the entire agricultural season. When comparing the  $T - \alpha$  with the  
586  $T - f_{vg}$  spaces, each polygon consistently describes the contour of the data  
587 points in both the  $T - \alpha$  and  $T - f_{vg}$  spaces. This justifies the approach for  
588 estimating temperature endmembers based on a synergistic use of  $T - \alpha$  and  
589  $T - f_{vg}$  spaces.

590 Given the previously retrieved four temperature endmembers, one is able  
591 to estimate the four component fractions at ASTER thermal sensor resolution  
592 over the 16 by 10 km area. Figure 10 presents the images of  $f_s$ ,  $f_{vgn}$ ,  $f_{vgn}$ ,  
593 and  $f_{vss}$  on each of the seven ASTER overpass dates. They illustrate both  
594 the seasonality of canopies throughout the agricultural period and the high  
595 variability of vegetation cover within the study area. The estimated fraction

596 of non-transpiring green vegetation ( $f_{vgn}$ ) is generally low over the irrigated  
597 area, with a mean maximum on 11 April before the senescence starts for the  
598 majority of crops.

### 599 5.2. Net radiation and ground heat flux

600 Figure 11 plots the simulated versus observed net radiation at the six  
601 flux stations. Since wheat is the dominant cropping type within the area,  
602 results for station 5 and 6 are highlighted with black markers. Statistics  
603 are reported in Table 3 in terms of correlation coefficient, root mean square  
604 difference, mean difference, and slope of the linear regression between simu-  
605 lated and observed data. A positive bias of  $24 \text{ Wm}^{-2}$  on  $Rn$  was found in  
606 Chirouze et al. (2013). In this paper, the absence of bias (estimated as  $-3$   
607  $\text{Wm}^{-2}$ ) on  $Rn$  can be explained by the use of ASTER-derived emissivity.  
608 The mean ASTER-derived  $\epsilon$  is about 0.95, which is significantly smaller than  
609 the default value (0.98) used in Chirouze et al. (2013). The slight difference  
610 in  $Rn$  estimates can also be explained by the fact that in this paper  $R_a$  was  
611 modeled using the formulation in Brutsaert (1975), whereas the observed  $R_a$   
612 was used in Chirouze et al. (2013).

613 Ground heat flux is computed as a fraction ( $\Gamma$  or  $\Gamma'$ ) of net radiation.  
614 In order to identify the impact on  $G$  of uncertainties in  $Rn$  and in  $\Gamma$  or  $\Gamma'$ ,  
615 four different expressions of  $G$  are derived using  $\Gamma$  or  $\Gamma'$ , and observed or  
616 simulated  $Rn$ . Figure 12 plots the simulated versus observed ground heat  
617 flux at the six flux stations, and error statistics are provided in Table 3.  
618 One observes that the  $\Gamma'$  formulation provides more accurate  $G$  estimates  
619 than the  $\Gamma$  formulation. Consequently, the explicit representation in SEB-  
620 4S of bare soil, its water status (via SEF), and unstressed green vegetation

621 helps model soil heat flux. By comparing the error statistics for  $G$  simulated  
622 using observed and simulated  $Rn$ , one observes that errors in modeled  $Rn$   
623 are responsible for a 10% error on simulated  $G$ .

624 Note that the slope of the linear regression between simulated and ob-  
625 served  $G$  is generally low. This can be explained by a significant overesti-  
626 mation of  $G$  measurements at station 3 (chickpea) (Chirouze et al., 2013).  
627 By removing data from station 3, the root mean square difference between  
628 simulated and observed  $G$  decreases from 46 to 34  $\text{Wm}^{-2}$  (for the case  $\Gamma'$   
629 and observed  $Rn$ ). The low slope of the linear regression between simulated  
630 and observed  $G$  can also be explained by uncertainties in  $f_s$  and SEF. Even  
631 if SEB-4S provides an estimate of  $f_s$  and SEF, it is worth reminding that  
632  $f_s$  is computed as the residual term of component fractions, which may in-  
633 tegrate several error sources, and SEF is computed from the retrieved soil  
634 temperature  $T_s$ , which systematically integrates errors in  $T_v$  estimated as  
635 the most probable (not the actual) vegetation temperature. In fact, bet-  
636 ter constraining soil heat fluxes would require knowledge of soil temperature  
637 (Moran et al., 1994), or soil evaporative efficiency or near-surface soil mois-  
638 ture (Merlin et al., 2012a).

639 The  $G$  formulation corresponding to  $\Gamma'$  and simulated  $Rn$  is used in the  
640 following subsections as the  $G$  component of all three (SEB-4S,  $T - \alpha$  image-  
641 based,  $T - f_{vg}$  image-based) surface energy balance models.

### 642 5.3. $ET$

643 Figure 13 plots the  $ET$  simulated by the  $T - \alpha$  image-based model, the  
644  $T - f_{vg}$  image-based, and SEB-4S versus measurements at the six stations.  
645 To quantify the impact of the modeling of available energy ( $Rn - G$ ) on  $ET$

646 predictions, Figures 13a,b,c present the ET modeled from the observed avail-  
647 able energy, and Figures 13d,e,f present the ET modeled from the modeled  
648 available energy. Error statistics are provided in Table 4 in terms of corre-  
649 lation coefficient, root mean square difference, mean difference, and slope of  
650 the linear regression between simulated and observed  $LE$ . One observes that  
651 uncertainties in modeled available energy slightly degrade model predictions,  
652 but the approach for estimating EF has a much more significant impact on  
653  $LE$  estimates. In terms of correlation coefficient for instance, modeled avail-  
654 able energy is responsible for a 0.00–0.03 difference, while modeled evapora-  
655 tive fraction is responsible for a 0.08–0.14 difference. Hence, improving EF  
656 representation is a key step in improving ET models. Overall, SEB-4S im-  
657 proves the correlation coefficient and slope of the linear regression between  
658 simulated and observed ET from 0.78-0.81 to 0.89, and from 0.55-0.63 to  
659 0.90, respectively. The improvement reaches about  $100 \text{ W m}^{-2}$  at low values  
660 and about  $100 \text{ W m}^{-2}$  at the seasonal peak of ET as compared with both  
661  $T - f_{vg}$  and  $T - \alpha$  image-based models.

662 Figure 14 presents the images on the seven ASTER overpass dates of  
663 the ET simulated by the  $T - \alpha$  image-based model, the  $T - f_{vg}$  image-  
664 based, and SEB-4S. A visual comparison indicates that the main differences  
665 between the three models occur during the second half of the agricultural  
666 season when the evaporative demand and the mean fraction of senescent  
667 vegetation are larger. The  $T - f_{vg}$  image-based model and SEB-4S have a  
668 similar behavior before the ET peak in April. However, significant differences  
669 between  $T - \alpha$  image-based model and SEB-4S are observable all along the  
670 agricultural season, including the period before the ET peak. Especially

671 the  $T - \alpha$  image-based model seems to lack sensitivity over the full ET  
672 range, thus systematically overestimating low values and underestimating  
673 large values. These differences are interpreted as resulting from the physical  
674 reasoning underlying the estimation of EF in each of the three models. In  
675 the  $T - \alpha$  image-based model, EF is computed by assuming that the wet  
676 surface edge is (CD) instead of [BC] in SEB-4S. In the  $T - f_{vg}$  image-based  
677 model, EF is computed by assuming that the energy fluxes over senescent  
678 vegetation behave as those over bare soil. In SEB-4S, EF is computed from  
679 on a consistent physical interpretation of both  $T - \alpha$  and  $T - f_{vg}$  spaces, and  
680 an explicit representation of four surface components including bare soil and  
681 senescent vegetation.

#### 682 5.4. Sensitivity to $\alpha_{vg}$ and $\alpha_{vs}$

683 In the current version of SEB-4S, the green and senescent vegetation albe-  
684 dos are set to constant values (0.19 and 0.39) for all crop types. One needs to  
685 assess the impact of variabilities (and uncertainties) in green and senescent  
686 vegetation albedos on ET estimates. A sensitivity analysis is undertaken by  
687 setting  $\alpha_{vg}$  and  $\alpha_{vs}$  to daily values. Daily  $\alpha_{vg}$  is estimated as the  $\alpha$  value  
688 corresponding to the minimum  $T$  on each date separately. Daily  $\alpha_{vs}$  is esti-  
689 mated as the maximum  $\alpha$  value observed on each date separately. The ET  
690 simulated by SEB-4S for each parameter set is then compared with the ET  
691 simulated using the constant  $\alpha_{vg}$  and  $\alpha_{vs}$  values (originally estimated as the  
692 average of daily  $\alpha_{vg}$ , and as the maximum value of daily  $\alpha_{vs}$  over the entire  
693 time series, respectively). The root mean square difference is estimated as  
694 24, 36 and 47  $\text{Wm}^{-2}$  in the case of daily  $\alpha_{vg}$  and constant  $\alpha_{vs}$ , daily  $\alpha_{vs}$   
695 and constant  $\alpha_{vg}$ , and both parameters estimated daily, respectively. When

696 comparing simulated ET with in situ measurements, the root mean square  
 697 difference and correlation coefficient are  $75 \text{ Wm}^{-2}$  and 0.92 for constant (orig-  
 698 inal) parameters,  $75 \text{ Wm}^{-2}$  and 0.92 for daily  $\alpha_{\text{vg}}$  and constant  $\alpha_{\text{vs}}$ ,  $87 \text{ Wm}^{-2}$   
 699 and 0.91 for constant  $\alpha_{\text{vg}}$  and daily  $\alpha_{\text{vs}}$ , and  $88 \text{ Wm}^{-2}$  and 0.91 for both  
 700 parameters estimated daily. To evaluate the impact of potential differences  
 701 of the albedo values ( $\alpha_{\text{vg}}$ ,  $\alpha_{\text{vs}}$ ) for different crops, an additional sensitivity  
 702 analysis is undertaken in space by artificially applying a Gaussian noise to  
 703  $\alpha_{\text{vg}}$  and  $\alpha_{\text{vs}}$  for each pixel independently. The noise amplitude (0.03 for  $\alpha_{\text{vg}}$   
 704 and 0.07 for  $\alpha_{\text{vs}}$ ) is set to the standard deviation over the entire time series  
 705 of the albedo endmembers estimated on a daily basis. The root mean square  
 706 difference between the ET simulated using original (undisturbed) parameters  
 707 and the ET simulated using the noised parameters is estimated as  $7 \text{ Wm}^{-2}$ .  
 708 Moreover, the root mean square difference and correlation coefficient between  
 709 simulated and observed ET is  $77 \text{ Wm}^{-2}$  and 0.91 for the noised dataset (as  
 710 compared with  $75 \text{ Wm}^{-2}$  and 0.92 for the original dataset). Hence the sensi-  
 711 tivity analysis reveals that 1) the assumption that  $\alpha_{\text{vg}}$  and  $\alpha_{\text{vs}}$  are relatively  
 712 constant is deemed acceptable in terms of simulated ET, and 2) SEB-4S is  
 713 quite robust with respect to uncertainties in  $\alpha_{\text{vg}}$  and  $\alpha_{\text{vs}}$ . In case a time  
 714 series of solar/thermal data is not available across the agricultural season,  
 715 estimating  $\alpha_{\text{vg}}$  and  $\alpha_{\text{vs}}$  on a daily basis seems to be a satisfying option.

## 716 6. Conclusions

717 An operational image-based surface energy balance model (SEB-4S) is  
 718 developed from a consistent physical interpretation of the polygons obtained  
 719 in the  $T - \alpha$  and  $T - f_{\text{vg}}$  spaces. The strength of the modeling approach

720 relies on the synergy between both  $T - \alpha$  and  $T - f_{vg}$  polygons. Specifically,  
721 the combination of  $T - \alpha$  and  $T - f_{vg}$  image-based approaches allows to  
722 explicitly separate the energy fluxes of four surface components of agricul-  
723 tural fields including bare soil, unstressed green vegetation, non-transpiring  
724 green vegetation, and standing senescent vegetation, and to robustly retrieve  
725 temperature endmembers regardless of crop phenological stages. SEB-4S op-  
726 erates in five steps: 1) estimating albedo and temperature endmembers, 2)  
727 estimating component temperatures, 3) estimating SEF, 4) estimating com-  
728 ponent fractions, and 5) computing component turbulent heat fluxes as a  
729 fraction of available energy.

730 To test the performance of SEB-4S, a  $T - \alpha$  image-based model and  
731 a  $T - f_{vg}$  image-based model are implemented as benchmarks. The three  
732 models are tested over a 16 km by 10 km irrigated area in northwestern  
733 Mexico during the 2007-2008 agricultural season. Input data are composed  
734 of ASTER thermal infrared, re-sampled Formosat-2 shortwave, and station-  
735 based meteorological data. The fluxes simulated by SEB-4S, the  $T - \alpha$   
736 image-based model, and the  $T - f_{vg}$  image-based model are compared on  
737 seven ASTER overpass dates with the in situ measurements collected at six  
738 locations in the study domain. The ET simulated by SEB-4S is significantly  
739 more accurate and robust than that predicted by the models based on a single  
740 (either  $T - f_{vg}$  or  $T - \alpha$ ) polygon. Overall, SEB-4S improves the correlation  
741 coefficient and slope of the linear regression between simulated and observed  
742 ET from 0.78-0.81 to 0.89, and from 0.55-0.63 to 0.90, respectively. The  
743 improvement reaches about  $100 \text{ W m}^{-2}$  at low values and about  $100 \text{ W}$   
744  $\text{m}^{-2}$  at the seasonal peak of ET as compared with both  $T - f_{vg}$  and  $T - \alpha$

745 image-based models. These differences result from the physical reasoning  
746 underlying the estimation of EF in each of the three models. In the  $T - \alpha$   
747 image-based model, EF is computed by assuming that the wet surface edge  
748 is the full-cover edge of the  $T - f_{vg}$  polygon. In the  $T - f_{vg}$  image-based  
749 model, EF is computed by assuming that the energy fluxes over senescent  
750 vegetation behave as those over bare soil. In SEB-4S, EF is computed from a  
751 consistent physical interpretation of the edges and vertices of both  $T - \alpha$  and  
752  $T - f_{vg}$  polygons, and an explicit representation of four surface components  
753 including bare soil and senescent vegetation.

754 In this paper, SEB-4S was successfully tested over a range of surface  
755 conditions in terms of ET. However, the energy partitioning between soil  
756 evaporation and plant transpiration was not directly validated over partially  
757 covered pixels. This point will be addressed in the near future using soil  
758 evaporation and plant transpiration measurements made independently from  
759 the tower ET observations. Although SEB-4S can be operationally applied  
760 to irrigated agricultural areas using ASTER or Landsat remote sensing data,  
761 several improvements are foreseen to extend its validity domain:

- 762 • Temperature endmembers: in this study, SEB-4S is applied to an irri-  
763 gated area including a large variability of soil moisture and vegetation  
764 cover conditions. Application to other less heterogeneous (e.g. rainfed  
765 agricultural) areas or to thermal data collected at coarser spatial res-  
766 olutions may induce significant uncertainties in temperature endmem-  
767 bers. To extend the validity domain of the temperature endmembers  
768 algorithm, one may constrain the minimum vegetation temperature by  
769 setting  $\mathbf{T}_{v,\min} = T_a$  (Merlin, 2013), and/or by using a formulation of

770 aerodynamic resistance.

- 771 • Representing the sensible heat flux of a wet surface: in the current  
772 version of SEB-4S, EF is assumed to be equal to EE. This means that  
773  $H_s$  and  $H_{vgu}$  for a well watered-surface are neglected and set to zero.  
774 Further studies may use a relationship between EF and EE.
  
- 775 • Linearity assumptions: SEB-4S is derived from a linearity assumption  
776 between EF and  $T$ , and a linearity assumption between  $T$  and  $T_s$ ,  $T_{vgu}$ ,  
777  $T_{vgn}$ , and  $T_{vss}$ . Moreover, the net radiation of surface components are  
778 simply expressed as a fraction of surface net radiation. The linearity  
779 assumptions are consistent with the image-based approaches, and are  
780 supported by the good results obtained in terms of ET estimates. How-  
781 ever, further studies should investigate step-by-step the validity of these  
782 assumptions. Especially, knowledge of component radiative properties  
783 (component emissivities, albedos, temperatures) may help improve the  
784 representation of surface fluxes.
  
- 785 • Soil heat and water fluxes: as indicated in the paper, better constrain-  
786 ing the soil (temperature and fraction) component would improve the  
787 estimation of soil heat and water fluxes. We will address this issue  
788 in future studies by integrating via a soil evaporative efficiency model  
789 (Merlin et al., 2011) the near-surface soil moisture derived from passive  
790 L-band SMOS (Kerr et al., 2010, Soil Moisture and Ocean Salinity)  
791 data and subsequently disaggregated at the thermal sensor resolution  
792 (Merlin et al., 2013) and/or a near-surface soil moisture index directly  
793 derived at high resolution from active C-band Sentinel-1 data.

794 **Acknowledgments**

795     The participants of the Yaqui 2007-2008 experiment are gratefully ac-  
796     knowledged. This study is part of the MIXMOD-E project funded by the  
797     French ANR (Agence Nationale de la Recherche).

798 **References**

- 799 Allen, R. G., Pereira, L. S., Raes, D., Smith, M., 1998. Crop evapotranspiration - Guidelines for computing crop water requirements. FAO Irrigation  
800 and drainage paper 56, FAO, Rome.
- 802 Anderson, M. C., Allen, R. G., Morse, A., Kustas, W. P., 2012.  
803 Use of Landsat thermal imagery in monitoring evapotranspiration  
804 and managing water resources. *Remote Sens. Environ.* 122, 50–65,  
805 doi:10.1016/j.rse.2011.08.025.
- 806 Anderson, M. C., Norman, J. M., Mecikalski, J. R., Otkin, J. A., Kus-  
807 tas, W. P., 2007. A climatological study of evapotranspiration and mois-  
808 ture stress across the continental united states based on thermal re-  
809 mote sensing: 1. model formulation. *J. Geophys. Res.* 112 (D10117),  
810 doi:10.1029/2006JD007506.
- 811 Bastiaanssen, W. G. M., Menenti, M., Feddes, R. A., Holtslag, A. A. M.,  
812 1998. A remote sensing surface energy balance algorithm for land (SEBAL)  
813 1. Formulation. *J. Hydrol.* 212-213, 198–212.
- 814 Bouilloud, L., Chancibault, K., Vincendon, B., Ducrocq, V., Habets, F.,  
815 Saulnier, G.-M., Anquetin, S., Martin, E., Noilhan, J., 2010. Coupling the  
816 ISBA land surface model and the TOPMODEL hydrological model for  
817 Mediterranean flash-flood forecasting: description, calibration, and vali-  
818 dation. *J. Hydrometeor.* 11, 315–333.
- 819 Boulet, G., Chehbouni, A., Gentine, P., Duchemin, B., Ezzahar, J., Hadria,

- 820 R., 2007. Monitoring water stress using time series of observed to un-  
821 stressed surface temperature difference. *Agri. For. Meteorol.* 146, 157–172.
- 822 Brutsaert, W., 1975. On a derivable formula for long-wave radiation from  
823 clear skies. *Water Resour. Res.* 11 (5), 742–744.
- 824 Bsaibes, A., Courault, D., Baret, F., Weiss, M., Olioso, A., Jacob, F.,  
825 Hagolle, O., Marloie, O., Bertrand, N., Desfond, V., Kzemipour, F., 2009.  
826 Albedo and LAI estimates from FORMOSAT-2 data for crop monitoring.  
827 *Remote Sens. Environ.* 113, 716–729, doi:10.1016/j.rse.2008.11.014.
- 828 Cammalleri, C., Anderson, M. C., Ciraolo, G., D’Urso, G., Kustas, W. P.,  
829 Loggia, G. L., Minacapilli, M., 2012. Applications of a remote sensing-  
830 based two-source energy balance algorithm for mapping surface fluxes  
831 without in situ air temperature observations. *Remote Sens. Environ.* 124,  
832 502–515, doi:10.1016/j.rse.2012.06.009.
- 833 Campbell, G., Norman, J., 1998. An introduction to environmental bio-  
834 physics, 2nd Edition. Springer, New York, USA.
- 835 Carlson, T. N., Gillies, R. R., Schmugge, T. J., 1995. An interpretation of  
836 methodologies for indirect measurement of soil water content. *Agri. For.*  
837 *Meteorol.* 77, 191–205.
- 838 Chern, J.-S., Ling, J., Weng, S.-L., 2008. Taiwan’s second re-  
839 mote sensing satellite. *Acta Astronautica* 63 (11-12), 1305–1311,  
840 doi:10.1016/j.actaastro.2008.05.022.
- 841 Chirouze, J., Boulet, G., Jarlan, L., Fieuzal, R., Rodriguez, J. C., Ezza-  
842 har, J., Er-raki, S., Bigeard, G., Merlin, O., Garatuza-Payan, J., Watts,

- 843 C., Chehbouni, G., 2013. Inter-comparison of four remote sensing based  
844 surface energy balance methods to retrieve surface evapotranspiration and  
845 water stress of irrigated fields in semi-arid climate. *Hydrol. Earth Syst.*  
846 *Sci. Discuss.* 10, 895–963, doi:10.5194/hessd-10-895-2013.
- 847 Choi, M., Kustas, W. P., Anderson, M. C., Allen, R. G., Li, F., Kjaers-  
848 gaard, J. H., 2009. An intercomparison of three remote sensing-based sur-  
849 face energy balance algorithms over a corn and soybean production re-  
850 gion (Iowa, U.S.) during SMACEX. *Agr. Forest Meteor.* 149, 2082–2097,  
851 doi:10.1016/j.agrformet.2009.07.002.
- 852 Cleugh, H., Leuning, R., Mu, Q., Running, S., 2007. Regional evaporation es-  
853 timates from flux tower and MODIS satellite data. *Remote Sens. Environ.*  
854 106, 285–304.
- 855 Courault, D., Seguin, B., Olioso, A., 2005. Review on estimation of evapo-  
856 transpiration from remote sensing data: from empirical to numerical mod-  
857 eling approaches. *Irrig. Drain. Syst.* 19, 223–249.
- 858 Fieuzal, R., Duchemin, B., Jarlan, L., Zribi, M., Baup, F., Merlin, O.,  
859 Hagolle, O., Garatuza-Payan, J., 2011. Combined use of optical and radar  
860 satellite data for the monitoring of irrigation and soil moisture of wheat  
861 crops. *Hydrol. Earth Syst. Sci.* 15, 1117–1129.
- 862 Findell, K. L., Gentine, P., Lintner, B. R., Kerr, C., 2011. Probability of  
863 afternoon precipitation in eastern United States and Mexico enhanced by  
864 high evaporation. *Nature Geosci.* 4, 434–439.

- 865 Galleguillos, M., Jacob, F., Prévot, L., French, A., Lagacherie, P., 2011.  
866 Comparison of two temperature differencing methods to estimate daily  
867 evapotranspiration over a Mediterranean vineyard watershed from ASTER  
868 data. *Remote Sens. Environ.* 115, 1326–1340.
- 869 Gillespie, A., Rokugawa, S., Matsunaga, T., Cothern, S., Hook, S., Khale,  
870 A., 1998. A temperature and emissivity separation algorithm for Advanced  
871 Spaceborne Thermal Emission and Reflection (ASTER) images. *IEEE*  
872 *Trans. Geosci. Remote Sens.* 36, 1113–1126.
- 873 Gonzalez-Dugo, M. P., Neale, C. M. U., Mateos, L., Kustas, W. P., Prueger,  
874 J. H., Anderson, M. C., Li, F., 2009. A comparison of operational remote  
875 sensing-based models for estimating crop evapotranspiration. *Agr. Forest*  
876 *Meteor.* 149, 1843–1853, doi:10.1016/j.agrformet.2009.06.012.
- 877 Gowda, P. H., Chavez, J. L., Colaizzi, P. D., Evett, S. R., Howell, T. A.,  
878 Tolk, J. A., 2008. ET mapping for agricultural water management: present  
879 status and challenges. *Irrig. Sci.* 26, 223–237, doi:10.1007/s00271-007-0088-  
880 6.
- 881 Gutman, G., Ignatov, A., 1998. The derivation of the green vegetation frac-  
882 tion from NOAA/AVHRR data for use in numerical weather prediction  
883 models. *Int. J. Remote Sens.* 19, 1533–1543.
- 884 Gutmann, E. D., Small, E. E., 2007. A comparison of land surface model  
885 soil hydraulic properties estimated by inverse modeling and pedotransfer  
886 functions. *Water Resour. Res.* 43 (W06520).

- 887 Hain, C., Mecikalski, J., Anderson, M., 2009. Retrieval of an available water-  
888 based soil moisture proxy from thermal infrared remote sensing. Part I:  
889 methodology and validation. *J. Hydrometeor.* 10, 665–683.
- 890 Hansen, V. F., 1993. *Albedos*. Vol. ARL-TR-57. Army Research Laboratory,  
891 US.
- 892 Idso, S. B., Jackson, R. D., Pinter, P. J., Reginato, R. J., Hatfield, J. L., 1981.  
893 Normalizing the stress-degree-day parameter for environmental variability.  
894 *Agric. Meteorol.* 24, 45–55.
- 895 Idso, S. B., Jackson, R. D., Reginato, R. J., Kimball, B. A., Nakayama, F. S.,  
896 1975. The dependence of soil albedo on soil water content. *J. Appl. Meteor.*  
897 14, 109–113.
- 898 Jackson, R. D., Idso, S. B., Reginato, R. J., Pinter, P. J., 1981. Canopy  
899 temperature as a crop water stress indicator. *Water Resour. Res.* 17 (4),  
900 1133–1138.
- 901 Jiang, L., Islam, S., 1999. A methodology for estimation of surface evapo-  
902 transpiration over large areas using remote sensing observations. *Geophys.*  
903 *Res. Lett.* 26, 2773–2776.
- 904 Kalma, J. D., McVicar, T. R., McCabe, M. F., 2008. Estimating land surface  
905 evaporation: a review of methods using remotely sensed surface tempera-  
906 ture data. *Surv. Geophys.* 29 (4-5), 421–469, doi:10.1007/s10712-008-9037-  
907 z.
- 908 Kerr, Y. H., Waldteufel, P., Wigneron, J.-P., Delwart, S., Cabot, F.,

- 909 Boutin, J., Escorihuela, M. J., Font, J., Reul, N., Gruhier, C., Ju-  
910 glea, S. E., Drinkwater, M. R., Hahne, A., Martin-Neira, M., Meck-  
911 lenburg, S., 2010. The SMOS mission: new tool for monitoring key  
912 elements of the global water cycle. In: IEEE. Vol. 98. pp. 666–687,  
913 doi:10.1109/JPROC.2010.2043032.
- 914 Kondratyev, K. Y., Korzov, V. I., Mukhenberg, V. V., Dyachenko, L. N.,  
915 1982. The shortwave albedo and the surface emissivity. P. S. Eagleson,  
916 Cambridge Univ. Press, UK.
- 917 Krapez, J.-C., Olioso, A., 2011. A combination of temperature, vegetation  
918 indexes and albedo, as obtained by airborne hyperspectral remote sensing,  
919 for the evaluation of soil moisture. *Quant. Infr. Thermog. J.* 8, 187–200,  
920 doi:10.3166/qirt.8.187-200.
- 921 Kustas, W. P., Anderson, M. C., 2009. Advances in thermal infrared remote  
922 sensing for land surface modeling. *Agr. Forest Meteor.* 149, 2071–2081,  
923 doi:10.1016/j.agrformet.2009.05.016.
- 924 Kustas, W. P., Daughtry, C. S. T., 1989. Estimation of the soil heat flux/net  
925 radiation ratio from spectral data. *Agr. For. Meteor.* 49, 205–223.
- 926 Long, D., Singh, V. P., 2012. A two-source trapezoid model for evapotranspi-  
927 ration (TTME) from satellite imagery. *Remote Sens. Environ.* 121, 370–  
928 388.
- 929 Long, D., Singh, V. P., Li, Z.-L., 2011. How sensitive is SEBAL to changes  
930 in input variables, domain sizes and satellite sensor? *J. Geophys. Res.*  
931 116 (D21107).

- 932 Long, D., Singh, V. P., Scalon, B. R., 2012. Deriving theoretical boundaries  
933 to address scale dependencies of triangle models for evapotranspiration  
934 estimation. *J. Geophys. Res.* 117 (D05113).
- 935 Matthias, A. D., Fimbres, A., Sano, E. E., Post, D. F., Accioly, L., Batchily,  
936 A. K., Ferreira, L. G., 2000. Surface roughness effects on soil albedo. *Soil*  
937 *Sci. Am. J.* 64, 1035–1041.
- 938 Menenti, M., Bastiaanssen, W., van Eick, D., Abd el Karim, M. A., 1989.  
939 Linear relationships between surface reflectance and temperature and their  
940 application to map actual evaporation of groundwater. *Adv. Space Res.*  
941 9 (1), 165–176.
- 942 Merlin, O., 2013. An original interpretation of the surface temperature-albedo  
943 space to estimate crop evapotranspiration (SEB-1S). *Hydrol. Earth Syst.*  
944 *Sci.Submitted*.
- 945 Merlin, O., Al Bitar, A., Rivalland, V., Béziat, P., Ceschia, E., Dedieu, G.,  
946 2011. An analytical model of evaporation efficiency for unsaturated soil  
947 surfaces with an arbitrary thickness. *J. Appl. Meteor. Clim.* 50 (2), 457–  
948 471, doi:10.1175/2010JAMC2418.1.
- 949 Merlin, O., Chehbouni, G., 2004. Different approaches in estimating heat  
950 flux using dual angle observations of radiative surface temperature. *Int. J.*  
951 *Remote Sens.* 25 (1), 275–289.
- 952 Merlin, O., Duchemin, B., Hagolle, O., Jacob, F., Coudert, B., Chehbouni,  
953 G., Dedieu, G., Garatuza, J., Kerr, Y., 2010. Disaggregation of MODIS  
954 Surface Temperature over an Agricultural Area Using a Time Series

- 955 of Formosat-2 Images. *Remote Sens. Environ.* 114 (11), 2500–2512,  
956 doi:10.1016/j.rse.2010.05.025.
- 957 Merlin, O., Escorihuela, M. J., Mayoral, M. A., Hagolle, O., Al Bitar,  
958 A., Kerr, Y., 2013. Self-calibrated evaporation-based disaggregation  
959 of SMOS soil moisture: an evaluation study at 3 km and 100 m  
960 resolution in Catalunya, Spain. *Remote Sens. Environ.* 130, 25–38,  
961 doi:10.1016/j.rse.2012.11.008.
- 962 Merlin, O., Jacob, F., Wigneron, J.-P., Walker, J., Chehbouni, G.,  
963 2012a. Multi-dimensional disaggregation of land surface temperature us-  
964 ing high-resolution red, near-infrared, shortwave-infrared and microwave-  
965 L bands. *IEEE Trans. Geosci. Remote Sens.* 50 (5), 1864–1880,  
966 doi:10.1109/TGRS.2011.2169802.
- 967 Merlin, O., Rüdiger, C., Al Bitar, A., Richaume, P., Walker, J.,  
968 Kerr, Y., 2012b. Disaggregation of SMOS soil moisture in southeast-  
969 ern Australia. *IEEE Trans. Geosci. Remote Sens.* 50 (5), 1556–1571,  
970 doi:10.1109/TGRS.2011.2175000.
- 971 Monteith, J. L., 1973. *Principles of environmental physics*. Edward Arnold  
972 Press.
- 973 Moran, M. S., Clarke, T. R., Inoue, Y., Vidal, A., 1994. Estimating crop wa-  
974 ter deficit using the relation between surface-air temperature and spectral  
975 vegetation index. *Remote Sens. Environ.* 49, 246–263.
- 976 Nagler, P. L., Inoue, Y., Glenn, E. P., Russ, A. L., Daughtry, C. S. T., 2003.

- 977 Cellulose absorption index (CAI) to quantify mixed soil-plant litter scenes.  
978 *Remote Sens. of Environ.* 87, 310–325.
- 979 Norman, J. M., Kustas, W. P., Humes, K. S., 1995. A two-source approach for  
980 estimating soil and vegetation energy fluxes in observations of directional  
981 radiometric surface temperature. *Agr. For. Meteorol.* 77, 263–293.
- 982 Ogawa, K., Schmugge, T., 2004. Mapping surface broadband emissivity of the  
983 Sahara desert using ASTER and MODIS data. *Earth Interactions* 8 (7),  
984 1–14.
- 985 Oki, T., Kanae, S., 2006. Global hydrological cycles and world water re-  
986 sources. *Science* 313, 1068–1072.
- 987 Piggin, I., Schwerdtfeger, P., 1973. Variations in the albedo of wheat and  
988 barley crops. *Arch. Met. Geoph. Biokl., Ser. B* 21, 365–391.
- 989 Prihodko, L., Goward, S. N., 1997. Estimation of air temperature from re-  
990 motely sensed surface observations. *Remote Sens. Environ.* 60, 335–346.
- 991 Roerink, G. J., Su, Z., Menenti, M., 2000. S-SEBI: a simple remote sens-  
992 ing algorithm to estimate the surface energy balance. *Phys. Chem. Earth*  
993 25 (2), 147–157.
- 994 Schmugge, T. J., Hook, S. J., Coll, C., 1998. Recovering surface temperature  
995 and emissivity from thermal infrared multispectral data. *Remote Sens.*  
996 *Environ.* 65, 121–131.
- 997 Seneviratne, S. I., Luthi, D., Litschi, M., Schar, C., 2006. Land-atmosphere  
998 coupling and climate change in Europe. *Nature* 443, 205–209.

- 999 Sheffield, J., Wood, E. F., 2008. Projected changes in drought occurrence  
1000 under future global warming from multi-model, multi-scenario, IPCC AR4  
1001 simulations. *Climate Dyn.* 31, 79–105.
- 1002 Su, Z., 2002. The Surface Energy Balance System (SEBS) for estimation of  
1003 turbulent heat fluxes. *Hydrol. Earth Syst. Sci.* 6 (1), 85–99.
- 1004 Tang, R., Li, Z.-L., Tang, B., 2010. An application of the Ts-VI method  
1005 with enhanced edges determination for evapotranspiration estimation from  
1006 MODIS data in arid and semi-arid regions: Implementation and validation.  
1007 *Remote Sens. Environ.* 114, 540–551, doi:10.1016/j.rse.2009.10.012.
- 1008 Tanguy, M., Baille, A., González-Real, M. M., Lloyd, C., Cappelaere, B.,  
1009 Kergoat, L., Cohard, J.-M., 2012. A new parameterisation scheme of  
1010 ground heat flux for land surface flux retrieval from remote sensing in-  
1011 formation. *J. Hydrol.* 454-455, 113–122, doi:10.1016/j.jhydrol.2012.06.002.
- 1012 Ten Berge, H., 1986. Heat and wave transfer at the bare soil surface. Aspects  
1013 affecting thermal imagery. PhD Thesis, Wageningen Univ., The Nether-  
1014 lands.
- 1015 Timmermans, W. J., Kustas, W. P., Anderson, M. C., French, A. N., 2007.  
1016 An intercomparison of the Surface Energy Balance Algorithm for Land  
1017 (SEBAL) and the Two-Source Energy Balance (TSEB) modeling schemes.  
1018 *Remote Sens. Environ.* 108, 369–384, doi:10.1016/j.rse.2006.11.028.
- 1019 Wallace, J. S., 2000. Increasing agricultural water use efficiency to meet  
1020 future food production. *Agr. Ecosyst. Environ.* 82, 105–119.

1021 Weiss, M., Baret, F., Leroy, M., Begué, A., Hautecoeur, O., Santer, R., 1999.  
1022 Hemispherical reflectance and albedo estimates from the accumulation of  
1023 across track sun synchronous satellite data. *J. Geophys. Res.* 104, 221–  
1024 232.

Table 1: Flux stations and instrumentation.

Station	Crop	$Rn$	$H$	$LE$	$G$
1	Safflower	CNR1	Young	KH2O	HFP-01
2	Chili Pepper	Q7	CSAT3	KH2O	HFP-01
3	Chickpea	Q7	CSAT3	KH2O	HFP-01
4	Potatoes - Sorghum	Q7	Young	KH2O	HFP-01
5	Wheat	CNR1	CSAT3	KH2O	HFP-01
6	Wheat	Q7	CSAT3	KH2O	HFP-01

Table 2: Definition of component fractions. Note that  $f_{vgu}$  and  $f_{vgn}$  are numerical (instead of analogical) representations of the water stress of green vegetation, which can be estimated as  $f_{vgn}/f_{vg}$ . For instance, a field crop undergoing a water stress of 0.5 within a given pixel would be represented by 50% of fully unstressed green vegetation ( $T_{vg} = \mathbf{T}_{v,\min}$ ) and 50% of non-transpiring vegetation ( $T_{vg} = \mathbf{T}_{v,\max}$ ).

Component fraction	Surface component	Component temperature
$f_s$	bare soil ( $= 1 - f_v$ )	$T_s$
$f_{vg}$	total green vegetation ( $= f_{vgu} + f_{vgn}$ )	$T_{vg}$
$f_{vgu}$	unstressed green vegetation	$\mathbf{T}_{v,\min}$
$f_{vgn}$	non-transpiring green vegetation	$\mathbf{T}_{v,\max}$
$f_{vss}$	standing senescent vegetation	$\mathbf{T}_{v,\max}$
$f_v$	total vegetation ( $= f_{vg} + f_{vss}$ )	$T_v$

Table 3: Correlation coefficient (R), root mean square difference (RMSD), bias and slope of the linear regression between simulated and observed  $Rn$  and  $G$  fluxes.

	$Rn$	$G/Rn$	R	RMSD	Bias	Slope
Flux	source	formulation	(-)	$Wm^{-2}$	$Wm^{-2}$	(-)
$Rn$	SEB-4S	NA	0.88	40	-3	0.87
$G$	Station	$\Gamma$	0.59	50	4	0.49
$G$	Station	$\Gamma'$	0.67	44	1	0.42
$G$	SEB-4S	$\Gamma$	0.51	54	2	0.40
$G$	SEB-4S	$\Gamma'$	0.59	48	-1	0.34

Table 4: Correlation coefficient (R), root mean square difference (RMSD), bias and slope of the linear regression between simulated and observed  $LE$  fluxes for the  $T - \alpha$  image-based model, the  $T - f_{vg}$  image-based model and SEB-4S and for observed and simulated available energy.

	$Rn\&G$	R	RMSD	Bias	Slope
Model	source	(-)	$Wm^{-2}$	$Wm^{-2}$	(-)
$T - \alpha$	Station	0.82	100	-17	0.63
$T - f_{vg}$	Station	0.78	110	12	0.56
SEB-4S	Station	0.92	75	-27	0.92
$T - \alpha$	SEB-4S	0.81	103	-16	0.63
$T - f_{vg}$	SEB-4S	0.78	110	12	0.55
SEB-4S	SEB-4S	0.89	85	-24	0.90

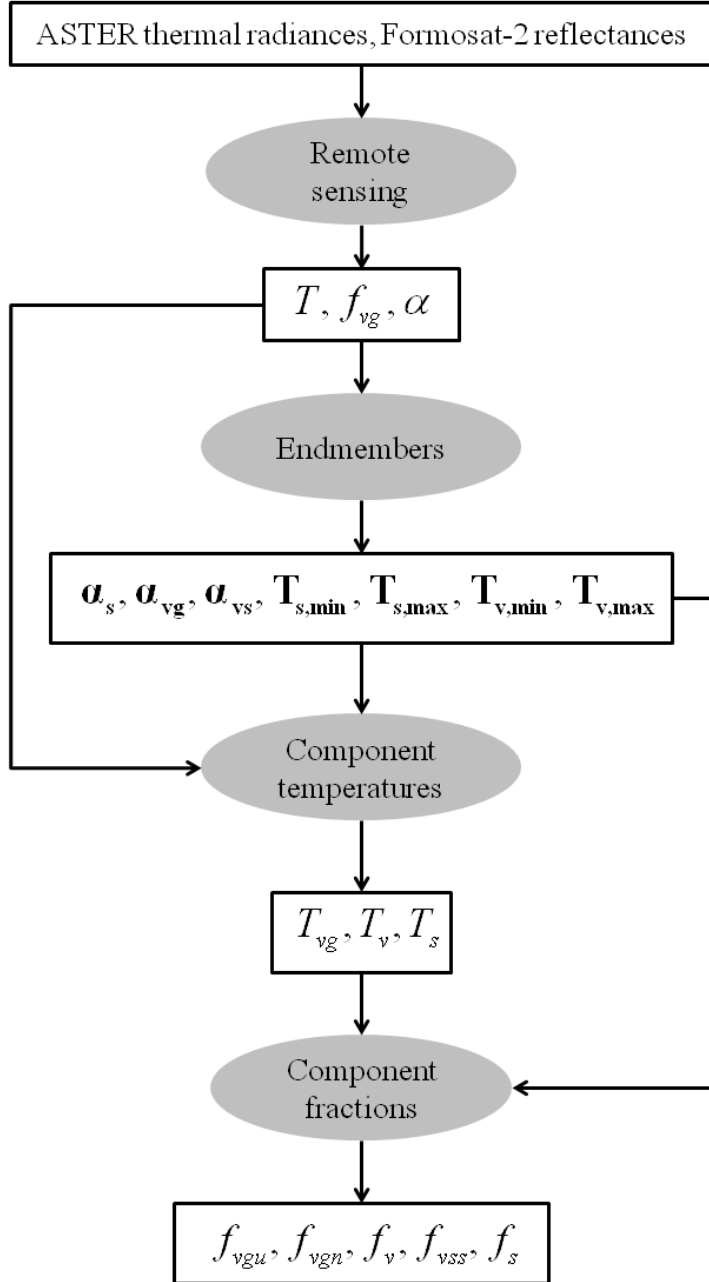


Figure 1: Data processing steps for determination of component fractions.

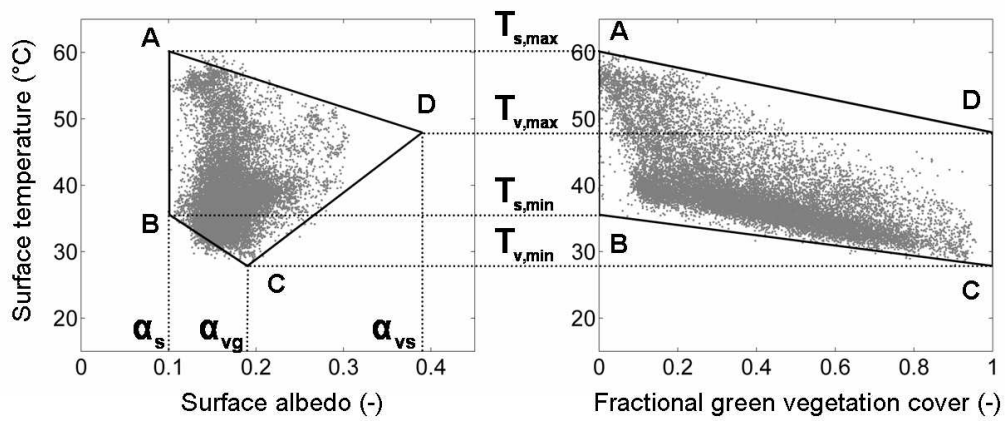


Figure 2: Consistent interpretation of the edges and vertices of the  $T - \alpha$  and  $T - f_{vg}$  polygons. Underlying grey points correspond to  $T$ ,  $\alpha$ , and  $f_{vg}$  data on 27 April 2008.

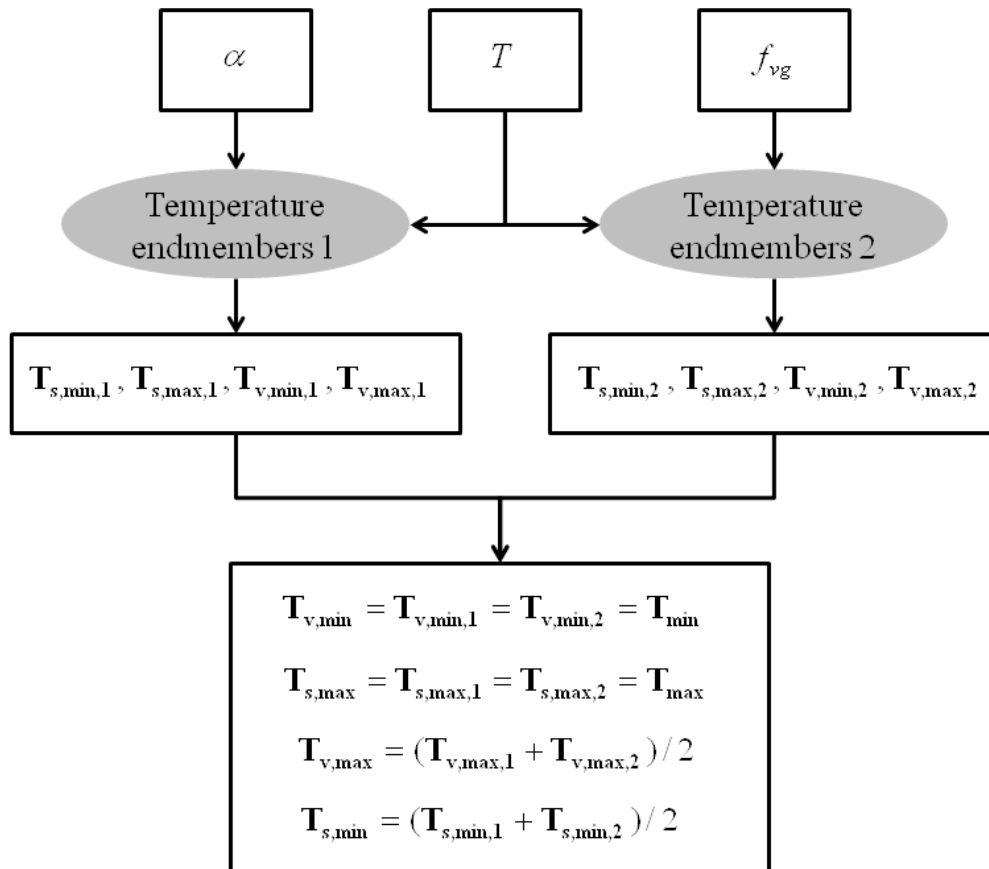


Figure 3: Data processing steps for determination of temperature endmembers.

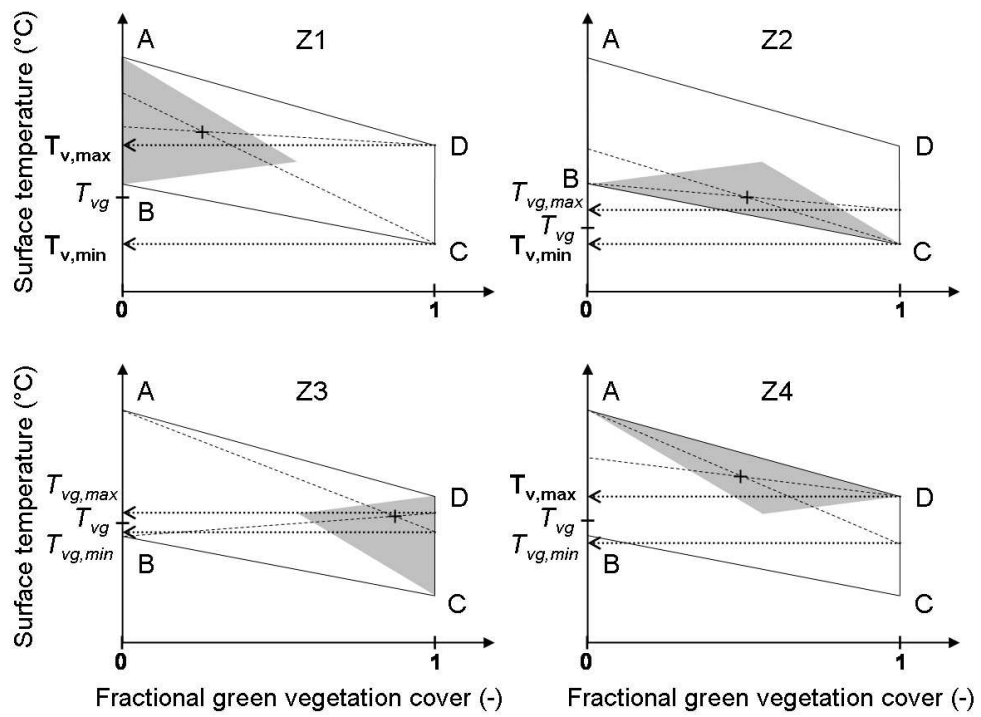


Figure 4: Most probable  $T_{vg}$  is estimated by applying the hourglass approach to the  $T-f_{vg}$  polygon.

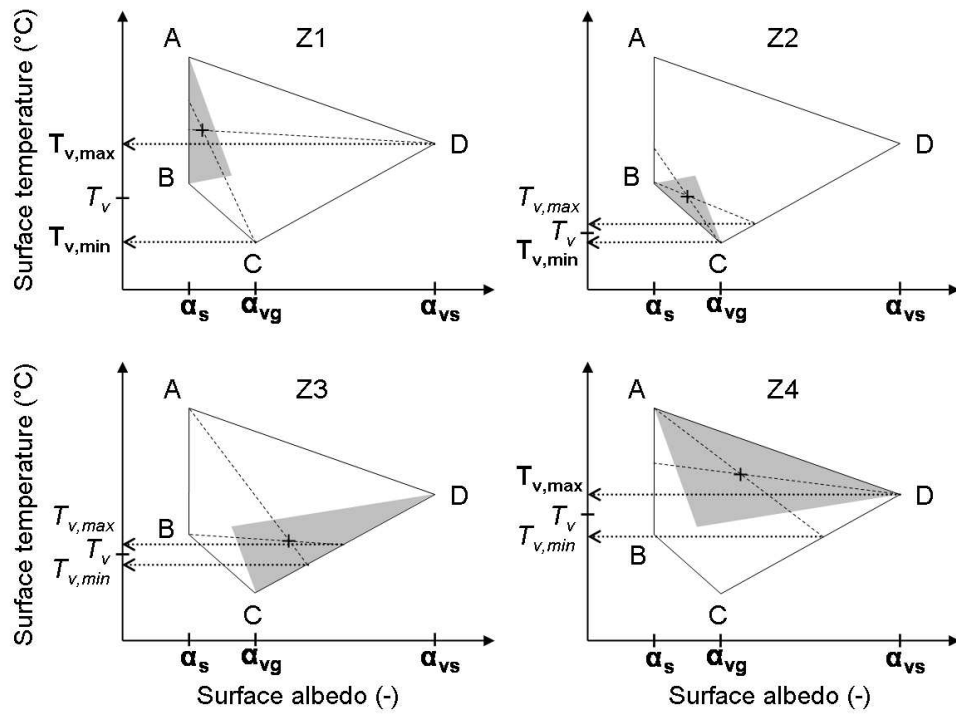


Figure 5: Most probable  $T_v$  is estimated by applying the hourglass approach to the  $T - \alpha$  polygon.

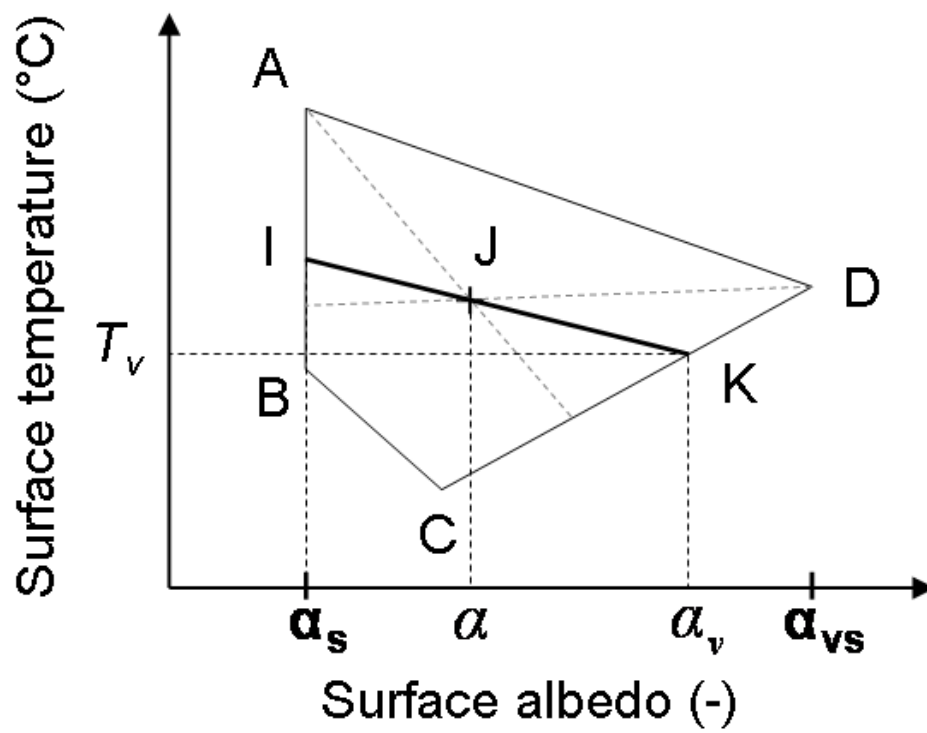


Figure 6:  $f_v$  is estimated as the ratio  $IJ/IK = (\alpha - \alpha_s)/(\alpha_v - \alpha_s)$ .

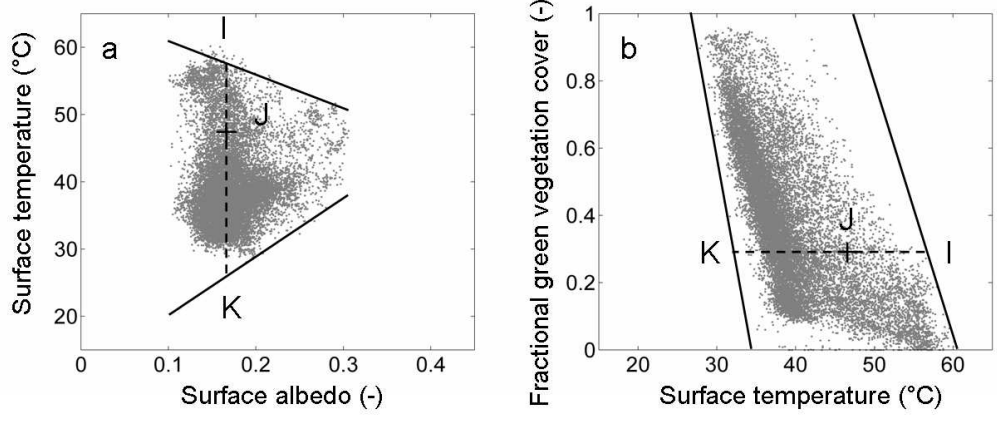


Figure 7: EF is computed as  $IJ/IK$  in the  $T - \alpha$  image-based (a) and the  $T - f_{vg}$  image-based (b) model.

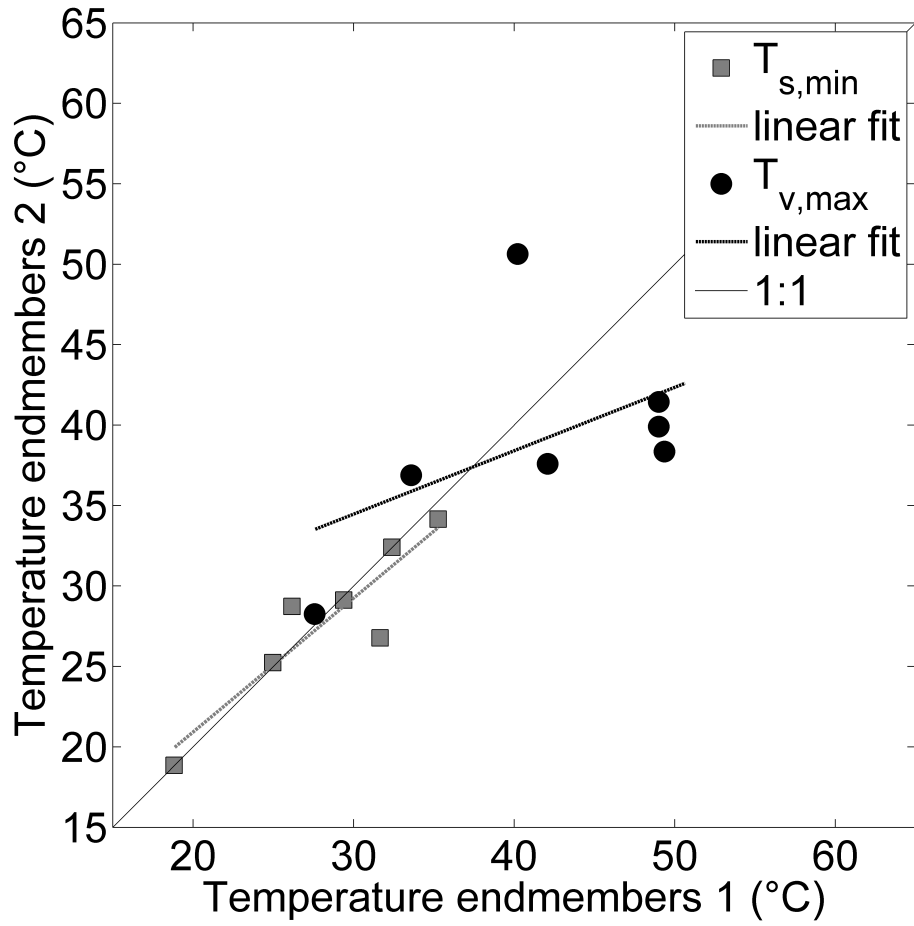


Figure 8: Temperature endmembers set 1 (derived from the  $T-\alpha$  space) and set 2 (derived from the  $T-f_{vg}$  space) are intercompared in terms of  $T_{s,min}$  and  $T_{v,max}$ .

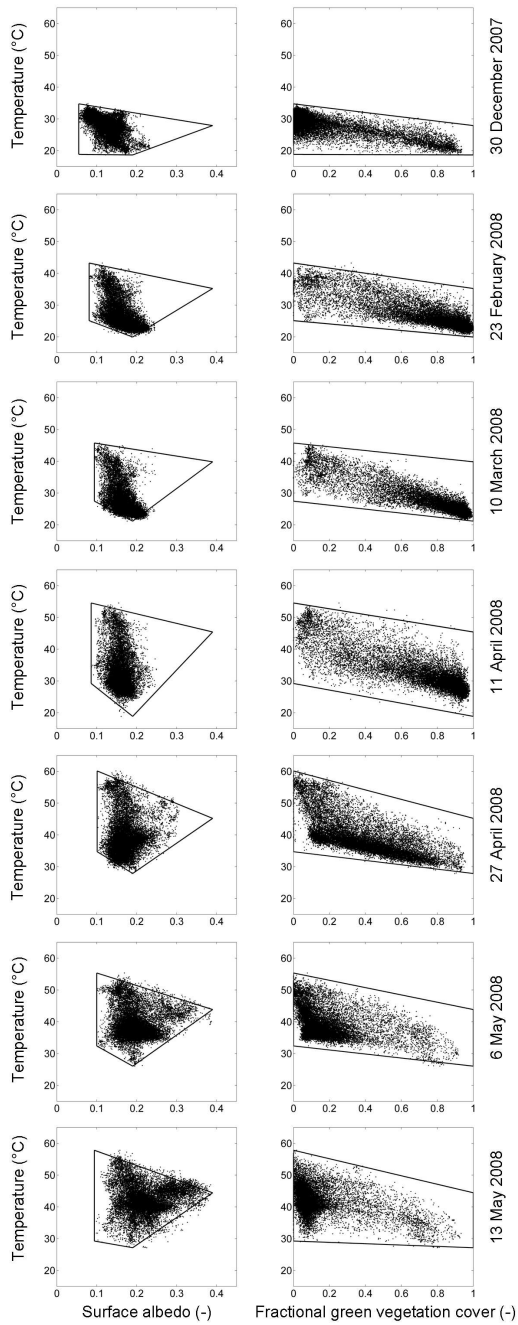


Figure 9: Estimating temperature endmembers by a consistent interpretation of the  $T - \alpha$  and  $T - f_{vg}$  spaces.

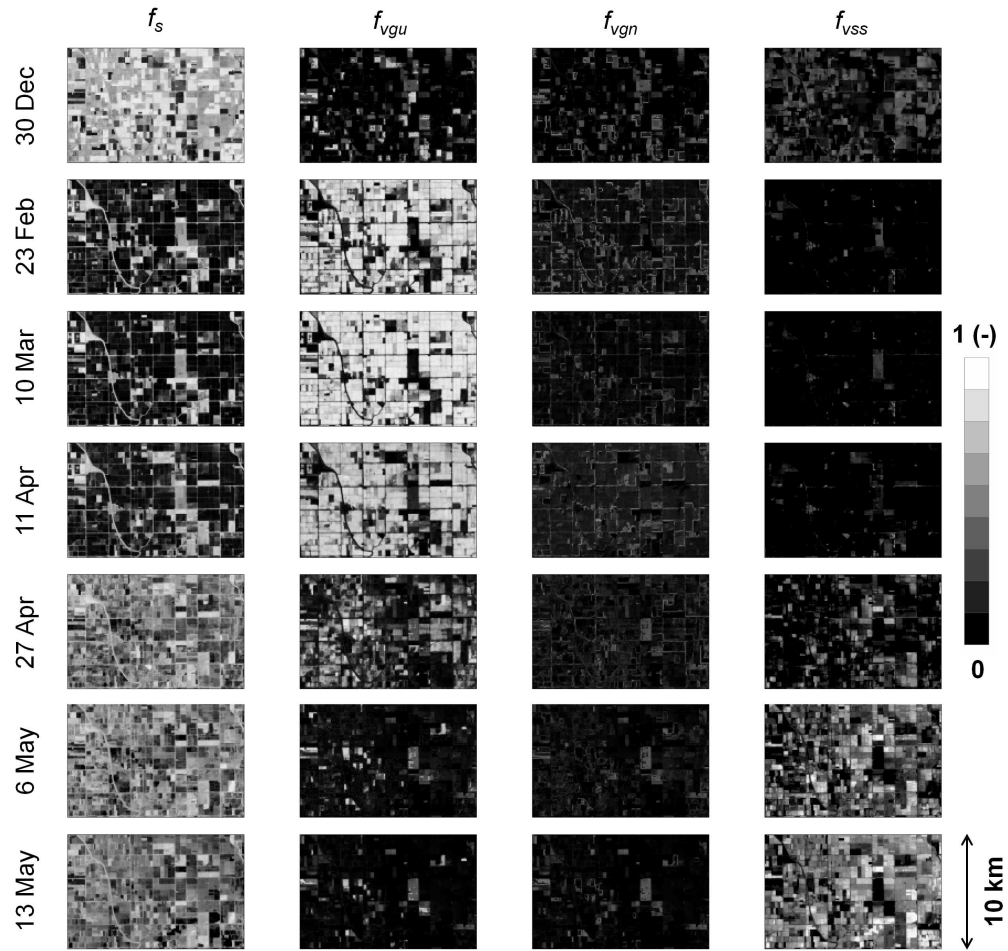


Figure 10: Component fractions on the seven ASTER overpass dates.

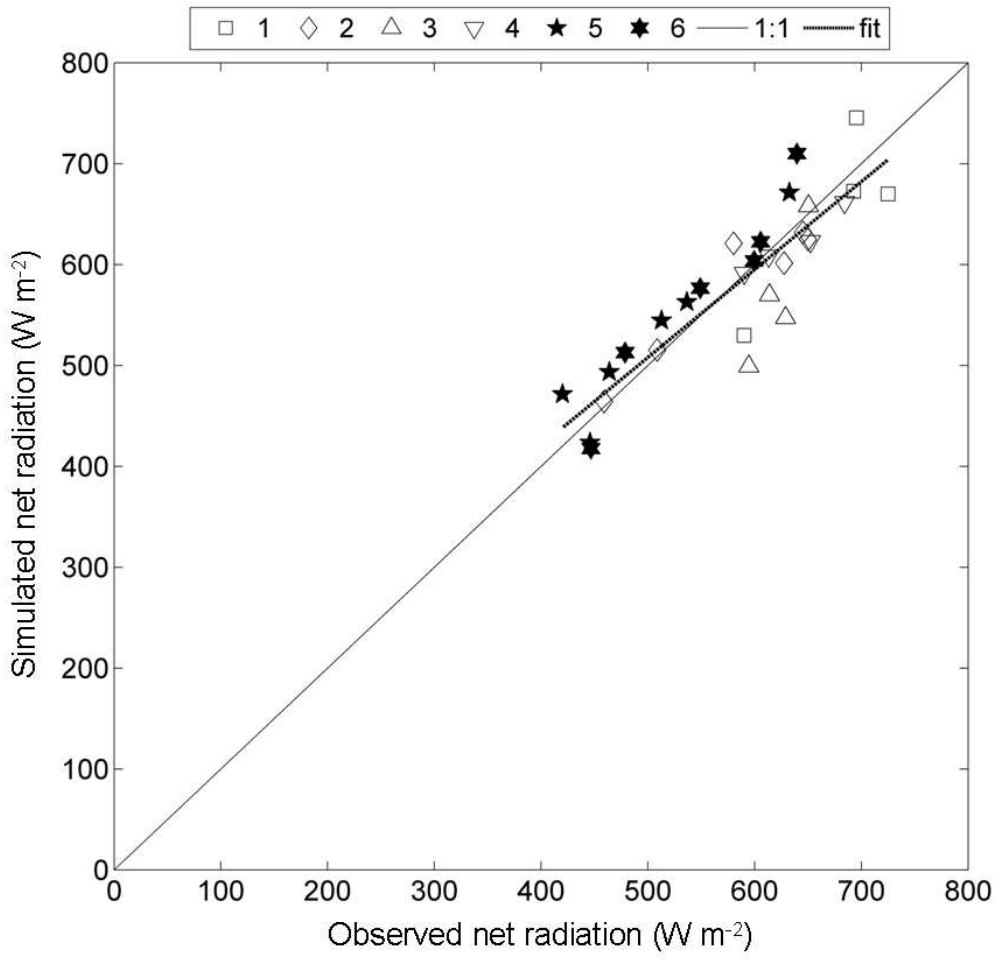


Figure 11: Modeled versus observed net radiation.

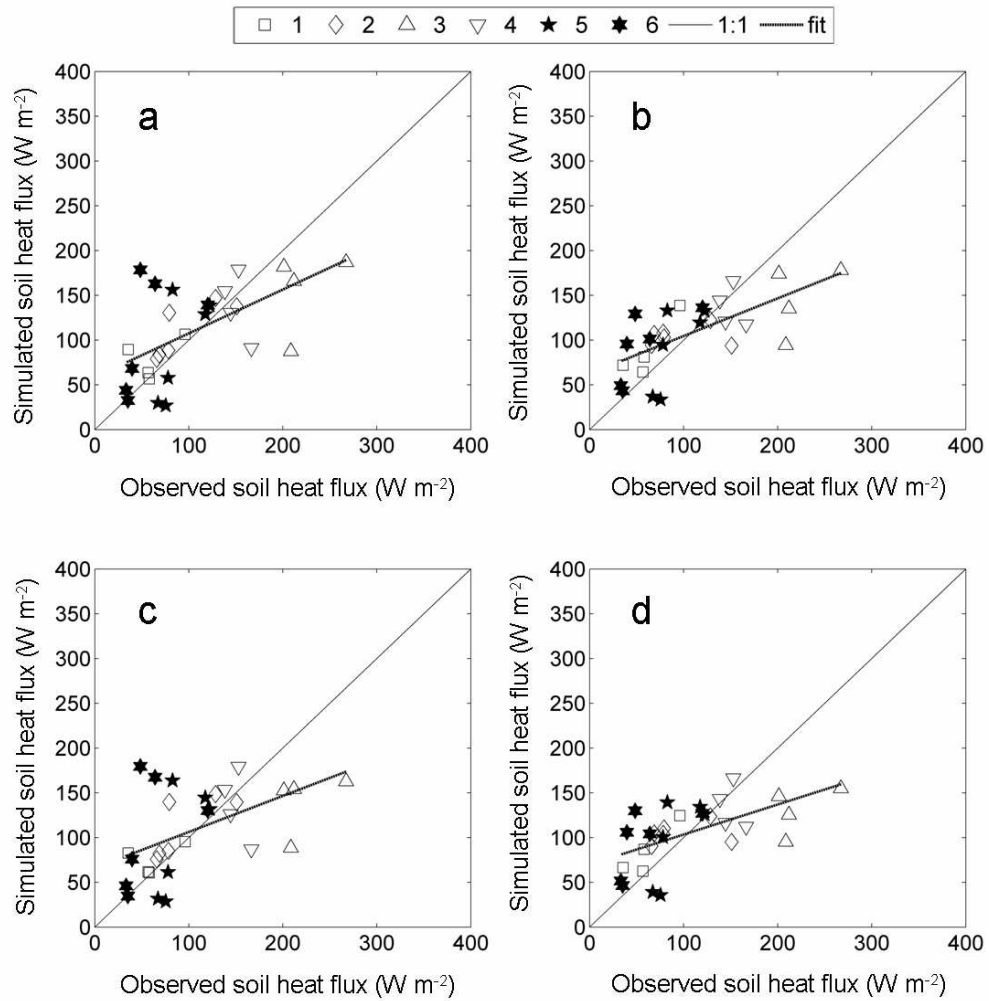


Figure 12: The ground heat flux simulated using  $\Gamma$  and observed  $Rn$  (a),  $\Gamma'$  and observed  $Rn$  (b),  $\Gamma$  and simulated  $Rn$  (c), and  $\Gamma'$  and simulated  $Rn$  (d) are plotted versus station measurements.

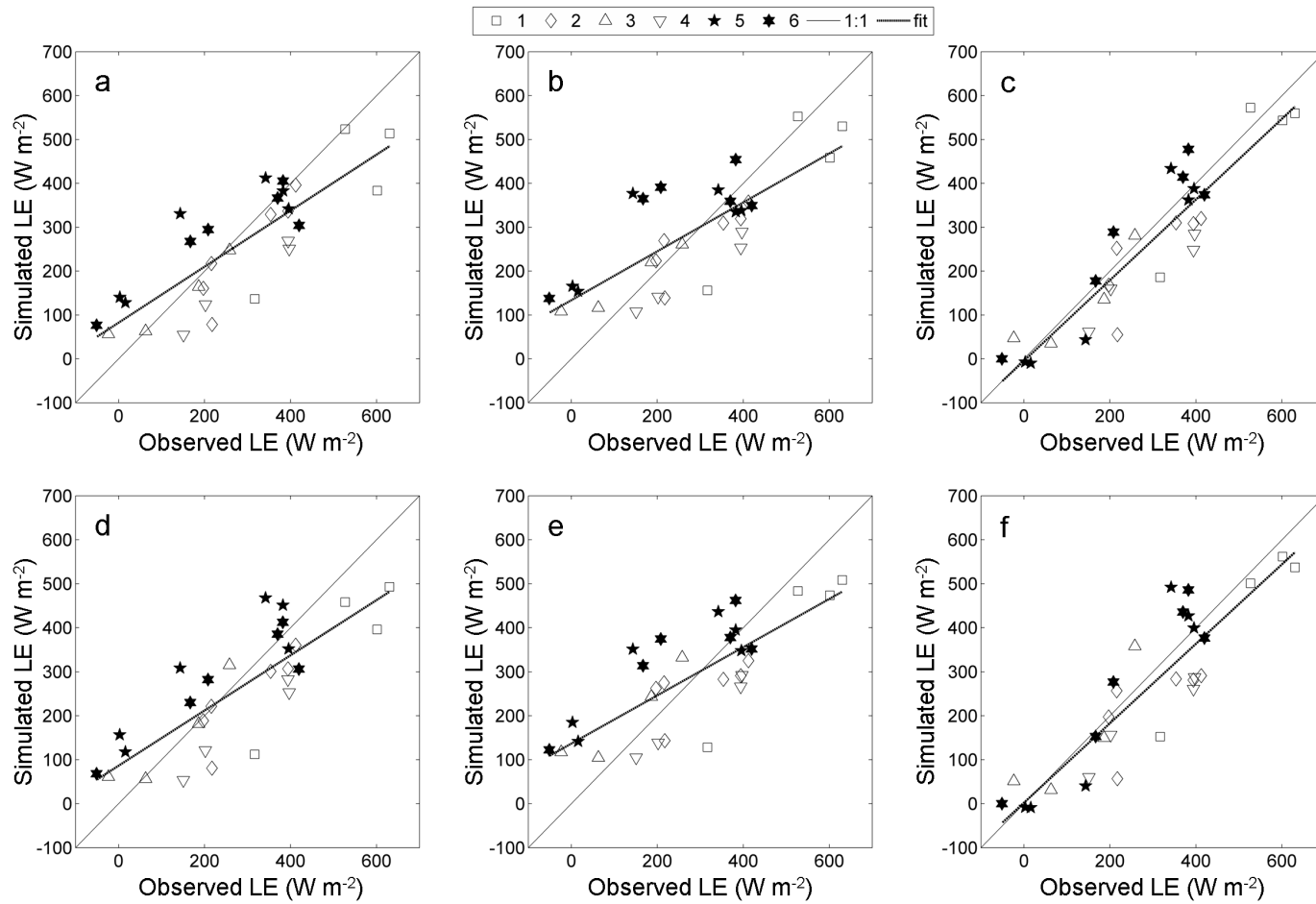


Figure 13: The ET simulated by the  $T - \alpha$  image-based model (left), the  $T - f_{vg}$  image-based model (middle), and SEB-4S (right) is plotted versus station measurements. The top line corresponds to data simulated using observed available energy ( $Rn - G$ ), and the bottom line corresponds to data simulated using modeled available energy.

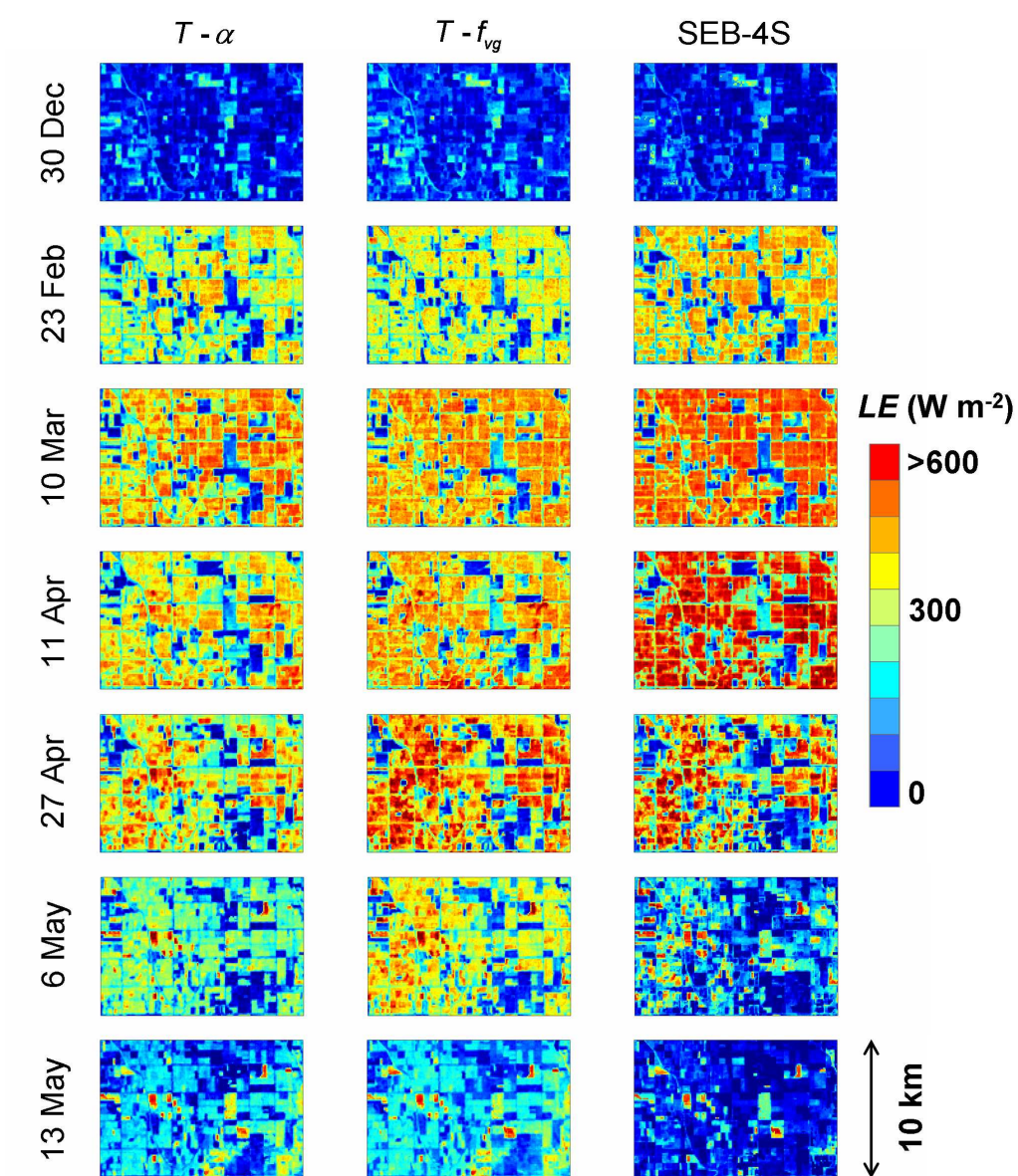


Figure 14: ET images simulated on the seven ASTER overpass dates by the  $T - \alpha$  image-based model, the  $T - f_{vg}$  image-based model, and SEB-4S.